# Global calculation of two-neutrino double-math xmlns="http://www.w3.org/1998/Math/MathML">mi>β/mi>/math> decay within the finite amplitude method in nuclear density functional theory

Nobuo Hinohara and Jonathan Engel

# Global calculation of two-neutrino double-beta decay
# with the finite amplitude method in nuclear density functional theory

Nobuo Hinohara[1, 2, *] and Jonathan Engel[3, †]

[1]*Center for Computational Sciences, University of Tsukuba, Tsukuba, 305-8577, Japan*
[2]*Faculty of Pure and Applied Sciences, University of Tsukuba, Tsukuba, 305-8571, Japan*
[3]*Department of Physics and Astronomy, University of North Carolina, Chapel Hill, North Carolina 27516-3255, USA*
(Dated: March 29, 2022)

Two-neutrino double-beta ($2\nu\beta\beta$) decay has been used to constrain the neutron-proton part of effective interactions, which in turn used to compute the nuclear matrix elements for neutrinoless double-beta decay, the observation of which would have important consequences for fundamental physics. We carefully examine $2\nu\beta\beta$ matrix elements within the proton-neutron quasiparticle random-phase approximation (pnQRPA) with nuclear energy density functionals (EDFs). We work with functionals that are fit globally to single-beta-decay half-lives and charge-exchange giant-resonance energies, but not to $2\nu\beta\beta$ half-lives themselves, to evaluate the $2\nu\beta\beta$ nuclear matrix elements for all important nuclei, including those whose half-lives have not yet been measured. Such a comprehensive evaluation in large model spaces without configuration truncation requires an efficient computational scheme; we employ a double contour integration within the finite-amplitude method. The results generally reproduce the nuclear matrix element extracted from half-lives well, without the use of any of those half-lives in the fitting procedure. We present predictions of the matrix elements in a total of 27 nuclei with half-lives that are still unmeasured.

## I. INTRODUCTION

Experiments all over the world are attempting to observe neutrinoless double-beta ($0\nu\beta\beta$) decay, which occurs only if neutrinos are Majorana particles, at a rate that is related to neutrino masses. To learn anything quantitative from an observed decay rate, one must know a nuclear matrix element that cannot be measured independently and so must be computed [1–4]. Such computations, which must handle the exchange of a virtual neutrino among nucleons and mesons, are difficult, and so the matrix elements for isotopes used in experiments are not known with high precision. A related process, two-neutrino double-beta ($2\nu\beta\beta$) decay, has been observed, however, and its rates are often a part of attempts to reduce the uncertainty in $0\nu\beta\beta$ nuclear matrix elements.

The $2\nu\beta\beta$ nuclear matrix elements have been extracted from measured half-lives in 11 nuclei at present [5]. To believe the results of many-body computations of $0\nu\beta\beta$ decay, one would like to see similar computations that reproduce these $2\nu\beta\beta$ matrix elements. Because the closure approximation — replacing the energies of states in the decay's intermediate nucleus with an average — is accurate for $0\nu\beta\beta$, some approaches rely on it and have a harder time with $2\nu\beta\beta$ decay, for which the approximation is poor. Nuclear density functional theory (DFT) in combination with the proton-neutron quasiparticle-random phase approximation (pnQRPA) is not one of these approaches, however; $0\nu\beta\beta$ and $2\nu\beta\beta$ matrix elements can be computed in similar ways. In many applications of the pnQRPA, in fact, the $2\nu\beta\beta$ matrix element is used to constrain the strength of the piece of the density functional associated with isoscalar proton-neutron pairing, which suppresses both the $0\nu\beta\beta$ and $2\nu\beta\beta$ matrix elements [6, 7].

The pnQRPA can be used in conjunction with a phenomenological Hamiltonian as well as in nuclear DFT. The advantage of DFT is its large single-particle model space and universality; a single energy-density functional (EDF) is taken to describe all the isotopes in the nuclear chart. The authors of Ref. [8] used a deformed-nucleus pnQRPA with a Skyrme EDF, computing $2\nu\beta\beta$ and $0\nu\beta\beta$ matrix elements in several experimentally important isotopes. They fit the strength of the isoscalar pairing interaction, on which rates depend sensitively, it obtains the correct $2\nu\beta\beta$ matrix elements before computing the $0\nu\beta\beta$ matrix elements.

Nuclear EDFs are commonly optimized to reproduce a number of experimental observables from a wide range of nuclei [9–14]. The optimization is easiest when the observables are ground-state expectation values in even-even isotopes. The time-odd part of the EDF and the proton-neutron pairing strength have no effect on even-even ground states, however, and so cannot be fixed in the same way. Instead, they are usually optimized globally, through the use of single-$\beta$-decay rates and Gamow-Teller and spin-dipole giant-resonance energies in nuclei all over the table of isotopes [15].

We would like to assess the ability of these globally determined EDFs to reproduce $2\nu\beta\beta$ matrix elements so that we can further optimize them if necessary and then confidently apply them to $0\nu\beta\beta$ decay. Standard pnQRPA calculations, however, require the construction of a QRPA matrix Hamiltonian, which within large single-particle spaces can consume too much computational time and memory. We can turn instead to the finite-amplitude method (FAM) within time-dependent DFT.

---

The FAM, which is formally equivalent to the QRPA [16, 17], computes the linear response induced by an external field with a complex frequency. One-body induced fields and the response of quasiparticle states are calculated by iteration, without the need to compute the two-body QRPA matrix elements. The proton-neutron version of the FAM (pnFAM) was developed and implemented in Ref. [18] in order to calculate $\beta$-decay rates and Gamow-Teller strength distributions [19, 20]. Because of its efficiency, it was used in Ref. [15] in an attempt to optimize the neutron-proton part of a particular nuclear EDF.

In this paper, we show how to use the pnFAM to efficiently compute $2\nu\beta\beta$ nuclear matrix elements. Our procedure, a preliminary version of which was reported on in Ref. [21], employs a complex-plane integration technique [22, 23] to perform the summation over intermediate states. We compare our $2\nu\beta\beta$ nuclear matrix elements in $^{76}$Ge, $^{130}$Te, $^{136}$Xe, and $^{150}$Nd to those obtained from matrix diagonalization with the same EDF in Ref. [8]. Then we use the EDFs with time-odd terms fit in Ref. [15] to compute the matrix elements for all 11 nuclei in which the $2\nu\beta\beta$ decay rate has been measured, and for 27 nuclei in which it has not.

The rest of this paper is organized as follows: Section II briefly presents the definition of the $2\nu\beta\beta$ matrix element and describes the pnQRPA. Section III formulates our scheme for computing $2\nu\beta\beta$ nuclear matrix elements in the pnFAM. Section IV compares the pnFAM $2\nu\beta\beta$ matrix elements with those obtained by matrix diagonalization in the pnQRPA, and Sec. V assesses the performance of globally fit functionals and offers predictions for unmeasured rates. Section VI is a conclusion.

## II. $2\nu\beta\beta$ MATRIX ELEMENT AND THE QRPA

### A. $2\nu\beta\beta$ matrix element

The nuclear matrix element governing the $2\nu\beta\beta$ decay of the nucleus $(N, Z)$ to the ground state of the nucleus $(N-2, Z+2)$ contributes to the half-life $T_{1/2}^{2\nu}$ as follows:

$$[T_{1/2}^{2\nu}]^{-1} = G_{2\nu}(Q_{\beta\beta}, Z)|M^{2\nu}|^2, \qquad (1)$$

where $G_{2\nu}$ is a phase space factor, and the $2\nu\beta\beta$ matrix element is a sum of Fermi and Gamow-Teller parts [1],

$$M^{2\nu} = M_{\text{GT}}^{2\nu} - \frac{g_V^2}{g_A^2} M_{\text{F}}^{2\nu}, \qquad (2)$$

$$M_{\text{F}}^{2\nu} = \sum_n \frac{\langle 0_f^+ | \sum_a \tau_a^- |n\rangle \langle n| \sum_b \tau_b^- |0_i^+\rangle}{E_n - \dfrac{M_i + M_f}{2}}, \qquad (3)$$

$$M_{\text{GT}}^{2\nu} = \sum_n \frac{\langle 0_f^+ | \sum_a \boldsymbol{\sigma}_a \tau_a^- |n\rangle \cdot \langle n| \sum_b \boldsymbol{\sigma}_b \tau_b^- |0_i^+\rangle}{E_n - \dfrac{M_i + M_f}{2}}. \qquad (4)$$

Here $\tau_a^-$ is the isospin-lowering operator for nucleon $a$, $\boldsymbol{\sigma}_a$ is the corresponding spin operator, $M_i$ and $M_f$ are the ground-state energies of the initial and final states of the decay (so that $Q_{\beta\beta} \equiv M_i - M_f$), and $|n\rangle$, with energy $E_n$ is one of a complete set of intermediate states in the nucleus $(N-1, Z+1)$. The Fermi part of the $2\nu\beta\beta$ matrix element is very small because isospin is nearly conserved [24], and we neglect it here.

### B. The pnQRPA

The proton-neutron QRPA evaluates the transition matrix elements between the initial or final state and the intermediate states that appear in the numerator of Eq. (4), taking into account the effect of the proton-neutron residual interaction beyond the mean-field approximation. In the pnQRPA, both the initial and final states $|0_{i/f,\text{QRPA}}^+\rangle$ are based on Hartree-Fock-Bogoliubov (HFB) quasiparticle vacua, which incorporate axially-symmetric deformation in our work. The intermediate states are related to the initial or final state by a QRPA phonon operator

$$|\lambda, K\rangle = \hat{Q}_K^{\lambda\dagger} |0_{\text{QRPA}}^+\rangle$$
$$\hat{Q}_K^{\lambda\dagger} = \sum_{\substack{pn \\ j_{z,p}+j_{z,n}=K}} X_{pn,K}^\lambda \hat{a}_p^\dagger \hat{a}_n^\dagger - Y_{pn,K}^\lambda \hat{a}_{\bar{n}} \hat{a}_{\bar{p}}, \qquad (5)$$

where $\hat{a}_{\tau=n,p}$ is a neutron or proton quasiparticle operator, defined so that $\hat{a}_\tau |0_{\text{HFB}}^+\rangle = 0$. Here, the indices $p$ and $n$ label proton and neutron quasiparticles. $j_{z,\tau}$ and $K$ are the projections along the symmetry axis of the quasiparticle and phonon angular momentum, and the index $\bar{\tau}$ labels the time-reversal partner of the state $\tau$ ($j_{z,\bar{\tau}} = -j_{z,\tau}$). From now on, for the sake of simplicity, we omit the restriction $j_{z,p} + j_{z,n} = K$ when summing over the proton and neutron quasiparticle states.

The QRPA amplitudes $X_{pn,K}^\lambda$ and $Y_{pn,K}^\lambda$ are solutions of the QRPA equations,

$$\sum_{p'n'} \begin{pmatrix} A_{pn,p'n'} & B_{pn,p'n'} \\ B_{pn,p'n'}^* & A_{pn,p'n'}^* \end{pmatrix} \begin{pmatrix} X_{p'n',K}^\lambda \\ Y_{p'n',K}^\lambda \end{pmatrix} = \Omega_K^\lambda \begin{pmatrix} X_{pn,K}^\lambda \\ -Y_{pn,K}^\lambda \end{pmatrix}, \qquad (6)$$

where $\Omega_K^\lambda$ is an excitation energy, measured from the QRPA ground state of the initial/final state. The $A$ and $B$ matrices contain residual interactions, computed from the second functional derivative of the EDF. The $2\nu\beta\beta$ matrix element can be calculated by combining the pnQRPA transition matrix elements from the initial and final states of the decay to the intermediate states. Because the procedure introduces two sets of the intermediate states, an additional approximation for matching them is necessary. We thus approximate the Gamow-Teller matrix element in Eq. (4) by

$$M_{\mathrm{GT}}^{2\nu} = \sum_{K=-1}^{1} (-1)^K \sum_{\substack{\lambda_i > 0 \\ \lambda_f > 0}} \frac{\langle 0_{f,\mathrm{QRPA}}^+ | \hat{F}_{-K}^{\mathrm{GT}-} | \lambda_f, K \rangle \langle \lambda_f, K | \lambda_i, K \rangle \langle \lambda_i, K | \hat{F}_{K}^{\mathrm{GT}-} | 0_{i,\mathrm{QRPA}}^+ \rangle}{\frac{\Omega_K^{\lambda_i} + \Omega_K^{\lambda_f}}{2}}. \tag{7}$$

In the summation, the expression $\lambda > 0$ denotes the states with $\Omega_K^\lambda > 0$.

The Gamow-Teller operator in the quasiparticle basis is

$$\hat{F}_K^{\mathrm{GT}\pm} = \sum_a (\sigma_K)_a \tau_a^\pm$$
$$= \sum_{pn} \left[ F_{20,K}^{\mathrm{GT}\pm}(pn) \hat{a}_p^\dagger \hat{a}_n^\dagger + F_{02,K}^{\mathrm{GT}\pm}(pn) \hat{a}_{\bar{n}} \hat{a}_{\bar{p}} \right]$$
$$+ (\hat{a}^\dagger \hat{a} - \mathrm{terms}), \tag{8}$$

and its transition amplitudes in Eq. (7) are given by

$$\langle \lambda_i, K | \hat{F}_K^{\mathrm{GT}-} | 0_{i,\mathrm{QRPA}}^+ \rangle =$$
$$\sum_{pn} \left[ F_{20,K}^{\mathrm{GT}-}(pn) X_{pn,K}^{\lambda_i *} + F_{02,K}^{\mathrm{GT}-}(pn) Y_{pn,K}^{\lambda_i *} \right]$$
$$\langle 0_{f,\mathrm{QRPA}}^+ | \hat{F}_{-K}^{\mathrm{GT}-} | \lambda_f, K \rangle =$$
$$\sum_{pn} \left[ F_{02,K}^{\mathrm{GT}-}(pn) X_{pn,K}^{\lambda_f} + F_{20,-K}^{\mathrm{GT}-}(pn) Y_{pn,-K}^{\lambda_f} \right]. \tag{9}$$

To compute the overlap of the two intermediate states $\langle \lambda_f, K | \lambda_i, K \rangle$ we adapt expressions based on the QRPA [25] and the quasiparticle Tamm-Dancoff approximation (QTDA) [8]. The result is

$$\langle \lambda_f, K | \lambda_i, K \rangle = \sum_{pnp'n'} \left( X_{p'n',K}^{\lambda_f *} X_{pn,K}^{\lambda_i} - \alpha Y_{p'n',K}^{\lambda_f *} Y_{pn,K}^{\lambda_i} \right)$$
$$\times \mathcal{O}_{pp'}(\alpha) \mathcal{O}_{nn'}(\alpha)$$
$$= \sum_{pn} \left( \bar{X}_{pn,K}^{\lambda_f *} \bar{X}_{pn,K}^{\lambda_i} - \alpha \bar{Y}_{pn,K}^{\lambda_f *} \bar{Y}_{pn,K}^{\lambda_i} \right), \tag{10}$$

where $\alpha$ is a parameter that is 0 for the QTDA overlap and 1 for the QRPA overlap, and the $\mathcal{O}_{\tau\tau'}(\alpha)$ are elements of the matrix that connects the quasiparticles associated with the initial and final states of the decay. Explicit expressions for these elements, together with the derivation of Eq. (10), are in Appendix A. $\bar{X}$ and $\bar{Y}$ are defined by

$$\bar{X}_{pn,K}^{\lambda_i} = \sum_{p'} \mathcal{O}_{pp'}^T(\alpha) X_{p'n,K}^{\lambda_i}, \tag{11a}$$

$$\bar{Y}_{pn,K}^{\lambda_i} = \sum_{p'} \mathcal{O}_{pp'}^T(\alpha) Y_{p'n,K}^{\lambda_i}, \tag{11b}$$

$$\bar{X}_{pn,K}^{\lambda_f} = \sum_{n'} X_{pn',K}^{\lambda_f} \mathcal{O}_{n'n}^T(\alpha), \tag{11c}$$

$$\bar{Y}_{pn,K}^{\lambda_f} = \sum_{n'} Y_{pn',K}^{\lambda_f} \mathcal{O}_{n'n}^T(\alpha). \tag{11d}$$

## III. THE FAM

### A. pnFAM

The FAM is formally equivalent to the QRPA and enables us to compute DFT response functions efficiently. A detailed formulation of the like-particle FAM and the pnFAM in the presence of the pairing correlations appear, respectively, in Refs. [17] and [18].

In the pnFAM, one applies a time-dependent external field of the form

$$\hat{F}_K^T(t) = \eta(\hat{F}_K^T e^{i\omega t} + \hat{F}_K^{T\dagger} e^{-i\omega t}), \tag{12}$$

with $\hat{F}_K^T$ a one-body proton-neutron excitation operator and $\omega$ a complex frequency. The excitation operator induces oscillations of quasiparticle annihilation operators (e.g. for neutrons) of the form

$$\delta\hat{a}_n(t) = \eta \sum_p \hat{a}_p^\dagger \left[ X_{pn}(\omega, \hat{F}_K^T) e^{-i\omega t} + Y_{pn}^*(\omega, \hat{F}_K^T) e^{i\omega t} \right]. \tag{13}$$

Solving the time-dependent DFT equations results in the FAM amplitudes $X_{pn}(\omega, \hat{F}_K^T)$ and $Y_{pn}(\omega, \hat{F}_K^T)$, which are related to the QRPA amplitudes $X_{pn,K}^\lambda$ and $Y_{pn,K}^\lambda$ through [22]

$$X_{pn}(\omega, \hat{F}_K^T) = -\sum_{\lambda > 0} \left\{ \frac{X_{pn,K}^\lambda \langle \lambda, K | \hat{F}_K^T | 0^+ \rangle}{\Omega_K^\lambda - \omega} \right.$$
$$\left. + \frac{Y_{pn,K}^{\lambda *} \langle 0^+ | \hat{F}_K^T | \lambda, -K \rangle}{\Omega_K^\lambda + \omega} \right\}, \tag{14}$$

$$Y_{pn}(\omega, \hat{F}_K^T) = -\sum_{\lambda > 0} \left\{ \frac{Y_{pn,K}^\lambda \langle \lambda, K | \hat{F}_K^T | 0^+ \rangle}{\Omega_K^\lambda - \omega} \right.$$
$$\left. + \frac{X_{pn,K}^{\lambda *} \langle 0^+ | \hat{F}_K^T | \lambda, -K \rangle}{\Omega_K^\lambda + \omega} \right\}. \tag{15}$$

### B. $2\nu\beta\beta$ matrix elements in the pnFAM

To calculate the QRPA $2\nu\beta\beta$ nuclear matrix element in Eq. (7), we separately solve the pnFAM computations in the initial and final nuclei, distinguishing quantities from the two nuclei with the superscripts $(i)$ and $(f)$. We then compute a quantity that is a combination of the
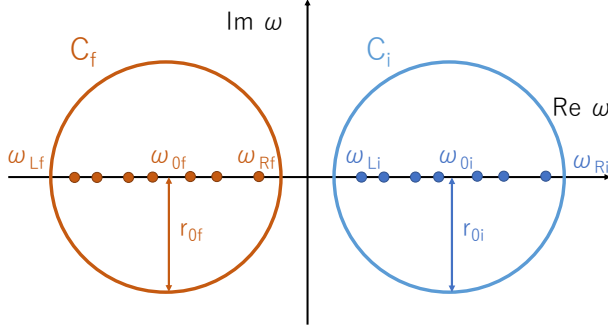
FIG. 1. Contours $C_i$ and $C_f$.

two sets of pnFAM amplitudes

$$\mathcal{T}(\alpha; \omega_i, \hat{F}_{K_i}^{T_i}; \omega_f, \hat{F}_{K_f}^{T_f}) \equiv \sum_{pn} \left[ \bar{Y}_{pn}^{(f)}(\omega_f, \hat{F}_{K_f}^{T_f}) \bar{X}_{pn}^{(i)}(\omega_i, \hat{F}_{K_i}^{T_i}) \right.$$
$$\left. - \alpha \bar{X}_{pn}^{(f)}(\omega_f, \hat{F}_{K_f}^{T_f}) \bar{Y}_{pn}^{(i)}(\omega_i, \hat{F}_{K_i}^{T_i}) \right],$$
(16)

where $\bar{X}^{(i/f)}$ and $\bar{Y}^{(i/f)}$ are the amplitudes in Eqs. (14) and (15), labeled in the same way as the QRPA amplitudes in Eq. (11). By substituting Eqs. (14) and (15) into Eq. (16), we obtain an expression for $\mathcal{T}$ in terms of the QRPA amplitudes:

$$\mathcal{T}(\alpha; \omega_i, \hat{F}_{K_i}^{T_i}; \omega_f, \hat{F}_{K_f}^{T_f}) = \sum_{pn} \sum_{\substack{\lambda_i > 0 \\ \lambda_f > 0}} \left[ \frac{(\bar{X}_{pn,K_f}^{\lambda_f *} \bar{X}_{pn,K_i}^{\lambda_i} - \alpha \bar{Y}_{pn,K_f}^{\lambda_f *} \bar{Y}_{pn,K_i}^{\lambda_i}) \langle 0_f^+ | \hat{F}_{K_f}^{T_f} | \lambda_f, -K_f \rangle \langle \lambda_i, K_i | \hat{F}_{K_i}^{T_i} | 0_i^+ \rangle}{(\Omega_{K_f}^{\lambda_f} + \omega_f)(\Omega_{K_i}^{\lambda_i} - \omega_i)} \right.$$

$$+ \frac{(\bar{Y}_{pn,K_f}^{\lambda_f *} \bar{X}_{pn,K_i}^{\lambda_i} - \alpha \bar{X}_{pn,K_f}^{\lambda_f *} \bar{Y}_{pn,K_i}^{\lambda_i}) \langle \lambda_f, K_f | \hat{F}_{K_f}^{T_f} | 0_f^+ \rangle \langle \lambda_i, K_i | \hat{F}_{K_i}^{T_i} | 0_i^+ \rangle}{(\Omega_{K_f}^{\lambda_f} - \omega_f)(\Omega_{K_i}^{\lambda_i} - \omega_i)}$$

$$+ \frac{(\bar{X}_{pn,K_f}^{\lambda_f *} \bar{Y}_{pn,K_i}^{\lambda_i} - \alpha \bar{Y}_{pn,K_f}^{\lambda_f *} \bar{X}_{pn,K_i}^{\lambda_i}) \langle 0_f^+ | \hat{F}_{K_f}^{T_f} | \lambda_f, -K_f \rangle \langle 0_i^+ | \hat{F}_{K_i}^{T_i} | \lambda_i, -K_i \rangle}{(\Omega_{K_f}^{\lambda_f} + \omega_f)(\Omega_{K_i}^{\lambda_i} + \omega_i)}$$

$$+ \left. \frac{(\bar{Y}_{pn,K_f}^{\lambda_f *} \bar{Y}_{pn,K_i}^{\lambda_i} - \alpha \bar{X}_{pn,K_f}^{\lambda_f *} \bar{X}_{pn,K_i}^{\lambda_i}) \langle \lambda_f, K_f | \hat{F}_{K_f}^{T_f} | 0_f^+ \rangle \langle 0_i^+ | \hat{F}_{K_i}^{T_i} | \lambda_i, -K_i \rangle}{(\Omega_{K_f}^{\lambda_f} - \omega_f)(\Omega_{K_i}^{\lambda_i} + \omega_i)} \right].$$
(17)

$\mathcal{T}$ has first-order poles at $\omega_i = \pm \Omega_{K_i}^{\lambda_i}$ and $\omega_f = \pm \Omega_{K_f}^{\lambda_f}$. We choose a counterclockwise contour $C_i$ ($C_f$) for $\omega_i$ ($\omega_f$) that includes positive-energy (negative-energy) poles and excludes all the negative-energy (positive-energy) poles, as in Fig. 1, to extract the residues from the first term on the right side of Eq. (17).

Integrating $\mathcal{T}$ together with an arbitrary regular complex function of $\omega_i$ and $\omega_f$ over those frequencies, we obtain an expression that can be used for two-body matrix elements:

$$\mathcal{M}(\alpha; \hat{F}_{K_i}^{T_i}, \hat{F}_{K_f}^{T_f}; f(\omega_i, \omega_f))$$

$$= -\frac{1}{4\pi^2} \oint_{C_i} d\omega_i \oint_{C_f} d\omega_f \mathcal{T}(\alpha; \omega_i, \hat{F}_{K_i}^{T_i}; \omega_f, \hat{F}_{K_f}^{T_f}) f(\omega_i, \omega_f)$$

$$= \sum_{\substack{\lambda_i > 0 \\ \lambda_f > 0}} \sum_{pn} \left( \bar{X}_{pn,K_f}^{\lambda_f *} \bar{X}_{pn,K_i}^{\lambda_i} - \alpha \bar{Y}_{pn,K_f}^{\lambda_f *} \bar{Y}_{pn,K_i}^{\lambda_i} \right)$$

$$\times f(\Omega_{K_i}^{\lambda_i}, -\Omega_{-K_f}^{\lambda_f}) \langle 0_f^+ | \hat{F}_{K_f}^{T_f} | \lambda_f, -K_f \rangle \langle \lambda_i, K_i | \hat{F}_{K_i}^{T_i} | 0_i^+ \rangle.$$
(18)

The Fermi and Gamow-Teller $2\nu\beta\beta$ decay nuclear matrix

elements are then given by

$$M_{\mathrm{F}}^{2\nu} = \mathcal{M}\left( \alpha; \hat{F}^{\mathrm{F}-}, \hat{F}^{\mathrm{F}-}; f = \frac{2}{\omega_i - \omega_f} \right),$$
(19)

$$M_{\mathrm{GT}}^{2\nu} = \sum_{K=-1}^{1} (-1)^K \mathcal{M}\left( \alpha; \hat{F}_K^{\mathrm{GT}-}, \hat{F}_{-K}^{\mathrm{GT}-}; f = \frac{2}{\omega_i - \omega_f} \right),$$
(20)

under the assumptions that $X_{-K}^{\lambda_f} = X_K^{\lambda_f}$, $Y_{-K}^{\lambda_f} = Y_K^{\lambda_f}$, and $\Omega_{-K_f}^{\lambda_f} = \Omega_{K_f}^{\lambda_f}$. Even when starting from the final state we use the external operator $\sigma_{-K} \tau^-$ that changes neutrons into protons to properly include the backward amplitudes in Eqs. (14) and (15).

By setting $f = 1$, $\alpha = 1$, and taking the same HFB vacuum for the initial and final states in Eq. (18), we can use that equation to compute the unweighted summed

TABLE I. Experimental values of $\tilde{\Delta}_n^{(3)}$ and $\tilde{\Delta}_p^{(3)}$ (in MeV) and the volume-pairing strengths $V_n$ and $V_p$ fit to those values (in MeV fm$^3$). The averages of the strengths in the initial and final nuclei used in the pairing EDF. Experimental binding energies are taken from Ref. [29]. Data in parentheses are not used to fit the pairing strengths.

| | $\tilde{\Delta}_n^{(3)}$ | $\tilde{\Delta}_p^{(3)}$ | $V_n$ | $V_p$ |
|---|---|---|---|---|
| $^{76}$Ge | 1.393 | 1.114 | $-182.70$ | $-194.49$ |
| $^{76}$Se | 1.551 | 1.392 | $-185.40$ | $-202.22$ |
| average | | | $-184.05$ | $-198.36$ |
| $^{130}$Te | 1.114 | (0.801) | $-166.21$ | N/A |
| $^{130}$Xe | 1.170 | 1.016 | $-173.80$ | $-194.00$ |
| average | | | $-170.01$ | $-194.00$ |
| $^{136}$Xe | (0.841) | 0.751 | N/A | $-148.66$ |
| $^{136}$Ba | 0.960 | 1.005 | $-184.16$ | $-172.54$ |
| average | | | $-184.16$ | $-160.60$ |
| $^{150}$Nd | 1.070 | 0.918 | $-181.64$ | $-202.31$ |
| $^{150}$Sm | 1.194 | 1.196 | $-184.84$ | $-195.24$ |
| average | | | $-183.24$ | $-198.78$ |

strengths:

$$\mathcal{M}^{i=f}(1; \hat{F}^{\mathrm{F}\mp}, \hat{F}^{\mathrm{F}\pm}; 1) = \sum_{\lambda>0} |\langle \lambda, 0|\hat{F}^{\mathrm{F}\mp}|0^+\rangle|^2, \quad (21)$$

$$\mathcal{M}^{i=f}(1; \hat{F}_K^{\mathrm{GT}\mp}, \hat{F}_{-K}^{\mathrm{GT}\pm}; 1) = (-1)^K \\ \times \sum_{\lambda>0} |\langle \lambda, K|\hat{F}_K^{\mathrm{GT}\mp}|0^+\rangle|^2. \quad (22)$$

Sum rules can be used to check the routines that compute matrix elements.

## IV. RESULTS WITH SKM* AND COMPARISON WITH PRIOR WORK

Our calculation of $2\nu\beta\beta$ nuclear matrix elements uses an extension of the pnFAM code developed in Ref. [18], which is in turn based on the nuclear DFT solver HFBTHO [26–28]. That last code uses the harmonic oscillator basis in a cylindrical coordinate system and allows axial deformation. In this section we provide details of our calculations with the SkM* functional and compare our $2\nu\beta\beta$ matrix elements for $^{76}$Ge, $^{130}$Te, $^{136}$Xe, and $^{150}$Nd with those obtained in Ref. [8] by diagonalizing the pnQRPA matrix.

### A. Parameter values

To integrate in cylindrical coordinates, we use Gauss-Hermite quadrature with $N_{\mathrm{GH}} = 40$ points for the $z$ direction, and Gauss-Laguerre quadrature with $N_{\mathrm{GL}} = 40$ points for the $r$ direction. To compute the direct Coulomb mean field, we use the prescription described in

Ref. [27] with length parameter $L = 50$ fm and $N_{\mathrm{Leg}} = 80$ Gauss-Legendre points.

We include $N_{\mathrm{sh}} = 20$ harmonic-oscillator major shells to describe the HFB wave functions. This corresponds to 1,771 single-particle states for neutrons and protons (with axial and time-reversal symmetry taken into account), and, in the pnFAM, to 257,686 $K = 0$ two-quasiparticle states and 256,025 $K = \pm 1$ two-quasiparticle states. We include all such states, with no additional model-space truncation, in the pnFAM calculations. The dimension of the pnQRPA matrix corresponding to our pnFAM calculations is about 500,000 for each $K$ quantum number.

We employ the same Skyrme SkM* functional [30] and volume-type pairing with 60 MeV energy cutoff (with $\hbar^2/2m = 20.73$ MeV fm$^2$ and the one-body center-of-mass correction included in the kinetic term) as that in Ref. [8]. The HFB solver cited in that paper, however, works in a cylindrical box with $r_{\max} = z_{\max} = 20$ fm and a coordinate spacing of 0.7 fm, and is thus different from ours.

We adjust the volume pairing strengths to reproduce experimental odd-even staggering (OES) with the density-averaged pairing gap. To reduce fluctuations [10], we take as the experimental data an average of the results of the three-point formula evaluated at the two even-odd

TABLE II. Properties of HFB ground states with the SkM* + volume pairing (with average pairing strengths) EDF. The table shows pairing gaps (in MeV), quadrupole deformation, and total HFB energies (in MeV), and compares the quadrupole deformation to the value in Ref. [8].

| | $\Delta_n$ | $\Delta_p$ | $\beta$ | $E_{\mathrm{HFB}}$ | $\beta$ (Ref [8]) |
|---|---|---|---|---|---|
| $^{76}$Ge | 1.609 | 1.473 | $-0.021$ | $-661.804$ | $-0.025$ |
| | 1.435 | 1.205 | 0.185 | $-662.274$ | 0.184 |
| | 1.612 | 1.475 | 0. | $-661.802$ | |
| $^{76}$Se | 1.589 | 1.648 | 0. | $-659.315$ | $-0.018$ |
| | 1.508 | 1.257 | $-0.194$ | $-659.594$ | |
| $^{130}$Te | 1.178 | 1.028 | 0. | $-1096.839$ | 0.01 |
| $^{130}$Xe | 1.078 | 1.009 | 0.141 | $-1093.423$ | 0.13 |
| | 1.107 | 1.113 | $-0.124$ | $-1093.152$ | |
| | 1.359 | 1.351 | 0. | $-1092.393$ | |
| $^{136}$Xe | 0. | 0.878 | 0. | $-1143.253$ | 0.004 |
| $^{136}$Ba | 1.025 | 0.931 | $-0.047$ | $-1139.268$ | $-0.021$ |
| | 0.928 | 0.735 | 0.094 | $-1139.538$ | |
| | 1.057 | 0.985 | 0. | $-1139.231$ | |
| $^{150}$Nd | 1.129 | 0.764 | 0.292 | $-1235.794$ | 0.27 |
| | 1.375 | 1.358 | $-0.177$ | $-1232.563$ | |
| | 1.422 | 1.688 | 0. | $-1231.080$ | |
| $^{150}$Sm | 1.131 | 1.307 | 0.223 | $-1234.675$ | 0.22 |
| | 1.294 | 1.707 | 0. | $-1232.436$ | |
| | 1.305 | 1.534 | $-0.137$ | $-1233.068$ | |

TABLE III. $Q$ values for each double-beta decay in units of MeV. Experimental $Q$ values are obtained from atomic masses [29].

|  | This paper | SkM* (Ref. [8]) | Exp. |
|---|---|---|---|
| $^{76}$Ge $\rightarrow$ $^{76}$Se | 4.05 | 4.84 | 2.04 |
| $^{130}$Te $\rightarrow$ $^{130}$Xe | 4.98 | 4.22 | 2.53 |
| $^{136}$Xe $\rightarrow$ $^{136}$Ba | 5.55 | 5.60 | 2.46 |
| $^{150}$Nd $\rightarrow$ $^{150}$Sm | 2.68 | 2.35 | 3.37 |

or odd-even systems:

$$
\tilde{\Delta}_n^{(3)}(N,Z) = \frac{\Delta_n^{(3)}(N-1,Z) + \Delta_n^{(3)}(N+1,Z)}{2}
$$
$$
\tilde{\Delta}_p^{(3)}(N,Z) = \frac{\Delta_p^{(3)}(N,Z-1) + \Delta_p^{(3)}(N,Z+1)}{2}, \tag{23}
$$

where $\Delta_{n/p}^{(3)}$ is the result of the three-point formula [31]. Table I lists the experimental values for this quantity, and the neutron and proton volume pairing strengths that best reproduce them. In order to use the same EDF for both nuclei in the decay, we take the average of the pairing strengths fit in the initial and final nuclei. We note that the experimental $\Delta_{n/p}^{(3)}$ values do not provide useful information if the series of isotopes used to calculate them includes closed-shell nuclei. $\Delta_p^{(3)}$ in $^{130}$Te ($Z = 50$ included) and $\Delta_n^{(3)}$ in $^{136}$Xe and $^{136}$Ba ($N = 82$ included) are such cases if the average of the results of two odd-even mass formulae is used. We avoid using the pairing gap $\tilde{\Delta}_p^{(3)}$ of $^{130}$Te to fit the proton pairing strength, fitting the pairing strength instead to the proton gap in $^{130}$Xe. We do adopt the neutron $\tilde{\Delta}^{(3)}$ of $^{136}$Ba, however, to determine the neutron pairing strength because the strengths fit to $\Delta_n^{(3)}$ and $\tilde{\Delta}_n^{(3)}$ are quite similar in that nucleus. The globally fit EDFs described in Sec. V are free from these problems.

Table II shows the results of the DFT calculations for the initial and final nuclei. The quadrupole deformations of the HFB states are quite close to those in Ref. [8]. We choose the HFB solution in the top line for each nucleus in which several HFB solutions coexist.

Table III shows $\beta\beta$ $Q$ values. Our calculation does not perfectly reproduce the values in Ref. [8], which were obtained from the same SkM* EDF but a different HFB code. We suspect that the differences are due to the different representations of the oscillator basis states and treatments of pairing.

Table IV lists the values of the HFB overlap included in the matrix $\mathcal{O}$. Our values agree with those of previous calculations with similar nuclear deformation. The overlap becomes small when the deformation of the initial and final states are different. That situation arises in $^{130}$Te and $^{136}$Xe, where the initial states are spherical while the final states are prolate and oblate, respectively. The overlap also becomes small when the initial or final state has no pairing gap. That is the case for neutrons

in $^{136}$Xe.

## B. Contour

To use the expression in Eq. (18), we must choose the contours $C_i$ and $C_f$. We take each to be centered on the real axis and circular, with the circle specified by the two energies $\omega_\mathrm{L}$ and $\omega_\mathrm{R}$ at they cross the real axis. The radius $r$ and the center of the contour $\omega_0$ are then given by $r = (\omega_\mathrm{R} - \omega_\mathrm{L})/2$ and $\omega_0 = (\omega_\mathrm{L} + \omega_\mathrm{R})/2$, and every point on the contour can be written in the form $\omega = \omega_0 + re^{i\theta}$. We use $\omega_\mathrm{L} = 0.1$ MeV and $\omega_\mathrm{R} = 120$ MeV for $C_i$ and $\omega_\mathrm{L} = -120$ MeV and $\omega_\mathrm{R} = -0.1$ MeV for $C_f$ to include all the unperturbed two-quasiparticle states within the quasiparticle-energy cutoff.

Figure 2 shows the integrands for the summed GT strength and the $2\nu\beta\beta$ matrix element in $^{76}$Ge as a function of the angle $\theta$ for the contour $C_i$. The main contribution to each comes from the peak at $\theta = \pi$, the point at $\omega = \omega_\mathrm{L}$ where the two contours are closest. While the integrand of the sum is distributed broadly along the whole contour $C_i$, the energy denominator $2/(\omega_i - \omega_f)$ concentrates the $2\nu\beta\beta$ contribution at $\theta = \pi$. To take this contribution into account precisely and efficiently, we introduce a parameter $\gamma$ to control the distribution of the discretized points near the origin, i.e., we discretize the angle $\theta$ as follows:

$$
\theta_k = (m + x_k^\gamma)\pi, \tag{24}
$$
$$
x_k = -1 + 2\frac{k-1}{n_r - 1} \quad (k = 1, 2, \cdots, n_r), \tag{25}
$$

where $\gamma$ is an odd number, and $m$ is 1 for $C_i$ and 0 for $C_f$. The parameter $\theta_k$ runs from 0 to $2\pi$ for $C_i$ and $-\pi$ to $\pi$ for $C_f$. We use $n_r = 202$ and omit the contribution from $(\omega_i, \omega_f) = (\omega_R, -\omega_L)$ because those points are on the real axis and can be very close to the QRPA poles, although their contribution to the nuclear matrix element should be small because of the factor $2/(\omega_i - \omega_f)$.

Table V shows the dependence of the summed strengths and the $2\nu\beta\beta$ matrix element in $^{76}$Ge on the parameter $\gamma$. The matrix element converges by $\gamma = 5$, which is the value we use.

TABLE IV. Neutron and proton parts of the HFB overlap $\langle 0_{f,\mathrm{HFB}}^+ | 0_{i,\mathrm{HFB}}^+ \rangle$ between the initial and the final states, compared with values from previous QRPA calculations.

|  | neutron | proton | total | Ref. [8] | Ref. [32] | Ref. [33] |
|---|---|---|---|---|---|---|
| $^{76}$Ge | 0.907 | 0.886 | 0.803 |  | 0.81 | 0.72, 0.73 |
| $^{130}$Te | 0.329 | 0.403 | 0.133 |  |  | 0.73, 0.73 |
| $^{136}$Xe | 0.480 | 0.787 | 0.378 | 0.47 |  | 0.43, 0.39 |
| $^{150}$Nd | 0.679 | 0.589 | 0.400 |  | 0.52 | 0.51, 0.52 |

TABLE V. Dependence on the discretization parameter $\gamma$ in $^{76}$Ge of summed Fermi and Gamow-Teller strengths $m(\text{F}\pm) = \sum_{\lambda>0} |\langle \lambda, 0|\hat{F}^{\text{F}\pm}|0^+\rangle|^2$ and $m(\text{GT}\pm) = \sum_K (-1)^K \sum_{\lambda>0} |\langle \lambda, K|\hat{F}_K^{\text{GT}\pm}|0^+\rangle|^2$ and of the dimensionless Gamow-Teller $2\nu\beta\beta$ nuclear matrix element. We use volume like-particle pairing and no isoscalar pairing.

| $\gamma$ | 1 | 3 | 5 | 7 |
|---|---|---|---|---|
| $m(\text{F}-)$ | 12.0213 | 12.0209 | 12.0201 | 12.0189 |
| $m(\text{F}+)$ | 0.0252 | 0.0255 | 0.0260 | 0.0269 |
| $m(\text{F}-) - m(\text{F}+)$ | 11.9961 | 11.9954 | 11.9940 | 11.9920 |
| $m(\text{GT}-)$ | 37.5860 | 37.5837 | 37.5811 | 37.5774 |
| $m(\text{GT}+)$ | 1.6065 | 1.6070 | 1.6085 | 1.6109 |
| $m(\text{GT}-) - m(\text{GT}+)$ | 35.9795 | 35.9767 | 35.9726 | 35.9664 |
| $M^{2\nu}m_ec^2$ | 0.1802 | 0.1574 | 0.1574 | 0.1575 |

### C. Summed Strengths

Table VI shows the unweighted summed Fermi and Gamow-Teller strengths obtained from the double contour integration for selected nuclei of interest to experimentalists. Integration up to 120 MeV reproduces more than 99.9% of the Ikeda sum rule in all these nuclei.

### D. $2\nu\beta\beta$ matrix element

We calculate the $2\nu\beta\beta$ matrix elements for $^{76}$Ge, $^{130}$Te, $^{136}$Xe, and $^{150}$Nd, setting the neutron-proton isovector pairing strength to the average of the neutron and proton like-particle pairing strengths ($V_1 = (V_n + V_p)/2$) and varying the isoscalar pairing strength $V_0$ from 0 to $-300$ MeV fm$^3$. We use the QTDA ($\alpha = 0$) to compute the overlap among intermediate states. Figure 3 displays the dependence of the $2\nu\beta\beta$ Gamow-Teller nuclear matrix elements on the isoscalar pairing strength. Like the authors of that paper, we use two values of $g_A$: one "unquenched" ($g_A = 1.25$, though the currently accepted
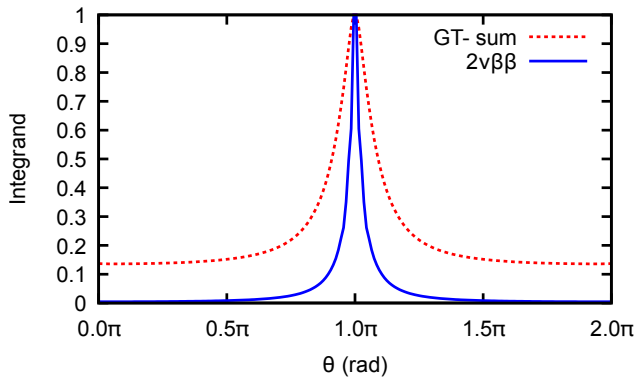


FIG. 2. Integrand in computation of summed Gamow-Teller strength and $2\nu\beta\beta$ matrix element for $^{76}$Ge, as a function of the angle $\theta$ for the contour $C_i$. The integrand is normalized to one at $\theta = \pi$.
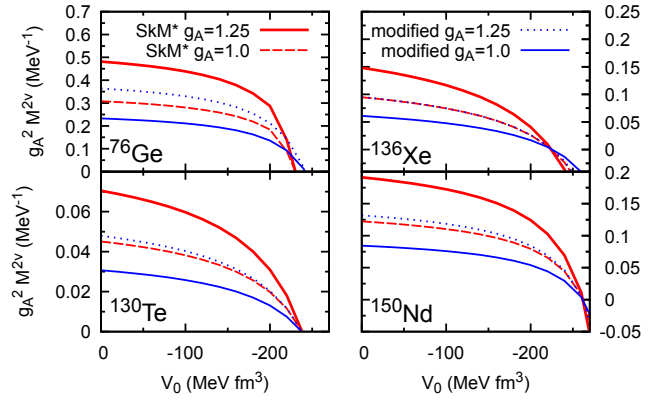


FIG. 3. Dependence on the isoscalar pairing strength of the $2\nu\beta\beta$ Gamow-Teller nuclear matrix element (in units of MeV$^{-1}$) for $^{76}$Ge, $^{130}$Te, $^{136}$Xe, and $^{150}$Nd, with the SkM* + volume pairing EDF. Red curves indicate the results with the time-odd functional derived from the SkM* interaction and blue curves the results with the modified time-odd functional. The thick solid and dotted curves correspond to $g_A = 1.25$, and the dashed and thin solid curves to the quenched value $g_A = 1.0$.

value is greater than 1.27) and one quenched ($g_A = 1.0$), and compare results for the EDF SkM* with and without a modified proton-neutron piece [$C_1^s = 100$ MeV fm$^3$, $C_1^T = C_1^{\nabla s} = 0$, see Eq. (26)]. Our matrix elements agree reasonably well with those of Ref. [8] in $^{130}$Te, $^{136}$Xe, and $^{150}$Nd, while they are about twice as large in $^{76}$Ge.

## V. GLOBAL EDF

### A. Performance of global EDFs

As Fig. 3 shows, the $2\nu\beta\beta$ and $0\nu\beta\beta$ nuclear matrix elements are suppressed by isoscalar proton-neutron pairing correlations that cannot be constrained from the ground-state properties of even-even nuclei. The usual QRPA approach uses $2\nu\beta\beta$ decay rates to determine the strength

TABLE VI. Summed Fermi and Gamow-Teller transitions, from double contour integration ($\omega_L = 0.1$ MeV and $\omega_R = 120$ MeV, $n_r = 202$, and $\gamma = 5$), as percentages of the corresponding sum rules.

| | $\dfrac{m(\text{F}-) - m(\text{F}+)}{N - Z}$ | $\dfrac{m(\text{GT}-) - m(\text{GT}+)}{3(N - Z)}$ |
|---|---|---|
| $^{76}$Ge | 0.9995 | 0.9992 |
| $^{76}$Se | 0.9994 | 0.9992 |
| $^{130}$Te | 0.9996 | 0.9993 |
| $^{130}$Xe | 0.9996 | 0.9993 |
| $^{136}$Xe | 0.9998 | 0.9997 |
| $^{136}$Ba | 0.9996 | 0.9994 |
| $^{150}$Nd | 0.9996 | 0.9994 |
| $^{150}$Sm | 0.9996 | 0.9995 |

of isoscalar pairing separately in each decaying nucleus. The philosophy of nuclear DFT, however, is that one EDF parameter set should, if possible, describe all the $\beta\beta$-decaying nuclei in the nuclear chart. In this subsection, we assess the ability of globally-fit EDFs to describe $2\nu\beta\beta$ decay, without using that observable at all in the fitting. We use Skyrme-type EDFs, with the isovector time-odd and isoscalar pairing parts globally fit to single-$\beta$ decay rates and to Gamow-Teller and spin-dipole resonances. Reference [15], which deals with single-$\beta$ decay in many isotopes, undertakes the global fitting and proposes ten parameter sets, called 1A, 1B, 1C, 1D, 1E, 2, 3A, 3B, 4, and 5, each corresponding to a different EDF. The time-even parts for all the sets except set 2 are taken from the functional SkO$'$ [34]; that of parameter set 2 comes from the functional SV-min [14] (though tensor-density terms are neglected, and the neutron and proton have different masses). In both cases, center-of-mass corrections to the mean field are neglected. The paper uses mixed volume-surface like-particle isovector pairing terms, fit to reproduce odd-even staggering in ten isotopes with $50 \leq A \leq 250$; the strengths are $V_n = -253.75$ MeV fm$^3$, $V_p = -274.68$ MeV fm$^3$ for SkO$'$ and $V_n = -244.06$ MeV fm$^3$, $V_p = -257.90$ MeV fm$^3$ for SV-min [35].

The isovector time-odd part of any Skyrme-type EDF is given by

$$\chi_1^{\text{odd}}(\boldsymbol{r}) = C_1^s[\rho_0]\boldsymbol{s}_1^2 + C_1^{\Delta s}\boldsymbol{s}_1 \cdot \Delta \boldsymbol{s}_1 + C_1^j \boldsymbol{j}_1^2$$
$$+ C_1^T \boldsymbol{s}_1 \cdot \boldsymbol{T}_1 + C_1^{\nabla j}\boldsymbol{s}_1 \cdot \boldsymbol{\nabla} \times \boldsymbol{j}_1$$
$$+ C_1^F \boldsymbol{s}_1 \cdot \boldsymbol{F}_1 + C_1^{\nabla s}(\boldsymbol{\nabla} \cdot \boldsymbol{s}_1)^2 , \qquad (26)$$

where $\boldsymbol{s}_1, \boldsymbol{j}_1, \boldsymbol{T}_1$, and $\boldsymbol{F}_1$ are the isovector spin, current, spin-kinetic, and tensor-kinetic densities, respectively. The isoscalar pairing functional in all these parameterizations has the mixed density dependence

$$\tilde{\chi}_0(\boldsymbol{r}) = \frac{V_0}{4}\left[1 - \frac{1}{2}\frac{\rho_0(\boldsymbol{r})}{\rho_c}\right]|\tilde{\boldsymbol{s}}_0(\boldsymbol{r})|^2 , \qquad (27)$$

where $\tilde{\boldsymbol{s}}_0$ is the isoscalar pair density, $\rho_c = 0.16$ fm$^{-3}$, and $\rho_0$ is the usual isoscalar density. In the parameter sets 1A, 1B, 1C, 1D, 1E, only $C_1^s$ (with no density dependence) and $V_0$ are fit. In sets 3A and 3B $C_1^T$ and $C_1^F$ are fit as well. In the parameter set 4, $C_1^j, C_1^{\nabla j}$, and $C_1^{\nabla s}$ are adjusted, while other parameters are the same as in set 3A. In set 5, $V_0, C_1^s$, and $C_1^j$ are fit.

Table VII lists the pairing gaps and quadrupole deformation of the HFB states used to compute $2\nu\beta\beta$ nuclear matrix elements. Neutron pairing collapses only in $^{136}$Xe and proton pairing collapses in $^{48}$Ca and $^{116}$Sn. SkO$'$ and SV-min cause different amounts of deformation. $^{96}$Zr, $^{100}$Mo, and $^{100}$Ru are oblate, oblate, and prolate (respectively) with SkO$'$, while they are all spherical with SV-min. $^{116}$Cd is spherical with SkO$'$, but is prolate with SV-min.

Table VIII contains the overlaps of the initial and final HFB vacua. Significant differences in deformation and pairing between the two HFB states lead to small

TABLE VII. The neutron and proton pairing gaps (in MeV) and quadrupole deformation for the lowest-energy HFB solutions in the initial and final nuclei of the decay, computed with the SkO$'$ and SV-min EDFs, together with a mixed pairing EDF. Solutions with parentheses are not the lowest-energy ones, but we use them in addition when calculating matrix elements.

| | SkO$'$ | | | SV-min | | |
|---|---|---|---|---|---|---|
| | $\Delta_n$ | $\Delta_p$ | $\beta$ | $\Delta_n$ | $\Delta_p$ | $\beta$ |
| $^{48}$Ca | 0.771 | 0.000 | 0.000 | 0.793 | 0.000 | 0.000 |
| $^{48}$Ti | 1.270 | 1.386 | 0.000 | 1.275 | 1.309 | 0.000 |
| $^{76}$Ge | 1.063 | 1.189 | 0.136 | 1.123 | 1.094 | 0.131 |
| $^{76}$Se | 1.134 | 1.532 | 0.000 | 1.165 | 1.352 | 0.000 |
| $^{82}$Se | 0.619 | 1.106 | 0.152 | 0.689 | 1.124 | 0.134 |
| $^{82}$Kr | 1.014 | 1.353 | 0.112 | 1.041 | 1.230 | 0.101 |
| $^{96}$Zr | 1.153 | 1.133 | −0.173 | 1.041 | 0.986 | 0.000 |
| | (1.354 | 1.129 | 0.000) | | | |
| $^{96}$Mo | 1.202 | 1.174 | 0.000 | 0.991 | 1.090 | 0.000 |
| $^{100}$Mo | 1.200 | 1.089 | −0.192 | 1.299 | 1.078 | 0.000 |
| | (1.123 | 1.246 | 0.214) | | | |
| $^{100}$Ru | 0.994 | 1.092 | 0.186 | 1.189 | 1.137 | 0.000 |
| $^{116}$Cd | 1.430 | 0.854 | 0.000 | 1.463 | 0.492 | 0.120 |
| $^{116}$Sn | 1.406 | 0.000 | 0.000 | 1.553 | 0.000 | 0.000 |
| $^{128}$Te | 1.139 | 0.970 | 0.000 | 1.209 | 0.907 | 0.000 |
| $^{128}$Xe | 1.136 | 0.912 | 0.142 | 1.152 | 0.841 | 0.156 |
| | (1.147 | 1.064 | −0.112) | (1.179 | 0.986 | −0.122) |
| $^{130}$Te | 1.013 | 0.971 | 0.000 | 1.043 | 0.902 | 0.000 |
| $^{130}$Xe | 1.051 | 1.001 | 0.111 | 1.077 | 0.947 | 0.118 |
| $^{136}$Xe | 0.000 | 1.180 | 0.000 | 0.000 | 1.143 | 0.000 |
| $^{136}$Ba | 0.767 | 1.349 | 0.000 | 0.775 | 1.296 | 0.000 |
| $^{150}$Nd | 0.962 | 0.686 | 0.311 | 0.886 | 0.830 | 0.266 |
| $^{150}$Sm | 0.901 | 1.074 | 0.238 | 0.823 | 1.101 | 0.203 |
| $^{238}$U | 0.863 | 0.735 | 0.265 | 0.763 | 0.596 | 0.269 |
| $^{238}$Pu | 0.828 | 0.640 | 0.269 | 0.745 | 0.572 | 0.272 |

overlaps, and because the two EDFs can produce different levels of deformation and pairing in any nucleus, the overlaps depend significantly on the EDF. In $^{96}$Zr and $^{100}$Mo, the HFB overlaps with SkO$'$ are extremely small because the initial state is oblate and the final state spherical or prolate. In $^{116}$Cd, the HFB overlap with SV-min is smaller for a similar reason. The QRPA may not be adequate when the overlaps, like those with SkO$'$ in $^{100}$Mo, are very small. Our treatment omits both projection onto states with good angular momentum, which involves the mixing of states with different orientations, and the fluctuation in shape and pairing captured, e.g., by the generator coordinate method [36, 37]. The effects of the physics we have neglected can be significant when the matrix elements are small at the HFB or QRPA levels.

In Fig. 4, we compare the Gamow-Teller $2\nu\beta\beta$ nuclear matrix element, scaled by $g_A^2 m_e c^2$ to be dimensionless, that result from calculations with the ten different SkO$'$- and SV-min-based EDFs discussed just above. We also show the experimental matrix elements, extracted from the half-lives in Ref. [5]. We use a quenched axial-vector coupling constant $g_A = 1.0$ to match the value from

TABLE VIII. The HFB overlap $\langle 0^+_{f,\text{HFB}}|0^+_{\text{HFB},i}\rangle$ between the initial and the final states of the double-beta decay, computed with SkO′ and SV-min EDFs. The numbers in parentheses denote powers of 10.

| | SkO′ | | | SV-min | | |
|---|---|---|---|---|---|---|
| | neutron | proton | total | neutron | proton | total |
| $^{48}$Ca | 0.764 | 0.513 | 0.392 | 0.776 | 0.512 | 0.398 |
| $^{76}$Ge | 0.577 | 0.559 | 0.323 | 0.586 | 0.587 | 0.344 |
| $^{82}$Se | 0.729 | 0.829 | 0.604 | 0.772 | 0.862 | 0.665 |
| $^{96}$Zr | 0.283 | 0.306 | 0.087 | 0.882 | 0.877 | 0.774 |
| (sph.→sph.) | 0.915 | 0.893 | 0.818 | | | |
| $^{100}$Mo | 1.8(−3) | 1.4(−2) | 2.6(−5) | 0.914 | 0.905 | 0.828 |
| (pro.→pro.) | 0.864 | 0.875 | 0.755 | | | |
| $^{116}$Cd | 0.932 | 0.521 | 0.485 | 0.507 | 0.293 | 0.148 |
| $^{128}$Te | 0.342 | 0.388 | 0.133 | 0.294 | 0.343 | 0.101 |
| (obl.$^{128}$Xe) | 0.440 | 0.533 | 0.235 | 0.403 | 0.487 | 0.197 |
| $^{130}$Te | 0.489 | 0.523 | 0.256 | 0.464 | 0.509 | 0.236 |
| $^{136}$Xe | 0.517 | 0.921 | 0.476 | 0.522 | 0.931 | 0.486 |
| $^{150}$Nd | 0.624 | 0.601 | 0.375 | 0.711 | 0.683 | 0.485 |
| $^{238}$U | 0.912 | 0.882 | 0.805 | 0.902 | 0.873 | 0.787 |
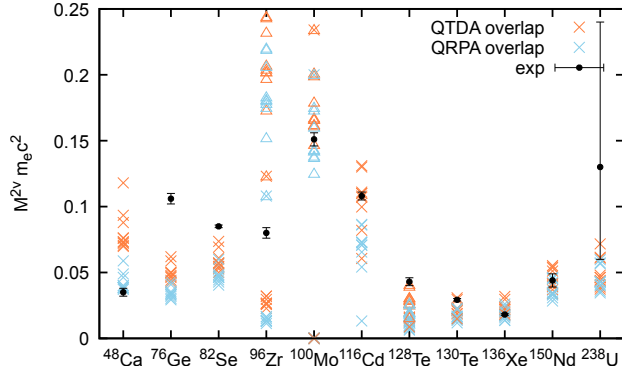


FIG. 4. Comparison of dimensionless $2\nu\beta\beta$ nuclear matrix elements obtained from global EDFs with experimental values. The matrix elements computed with the lowest-energy HFB solutions are marked with crosses, while those elements computed with the other HFB solutions are marked with triangles. Orange symbols come from computations with the QTDA overlap and blue symbols from computations with the QRPA overlap. The EDFs that give rise to each particular point appear in Table IX in Appendix B.

Ref. [15], which determines the EDF parameters. Despite the differences among the EDFs in the pieces of the functional that were fit and in the data chosen to fit them, the $2\nu\beta\beta$ matrix elements that they produce are quite close to one another in some of the heavier nuclei. This fact means that the parts of the EDF that affect the $2\nu\beta\beta$ matrix element are determined almost fully by the $\beta$ decay rates and giant resonance energies used in fitting them. In some lighter isotopes such as $^{48}$Ca, $^{96}$Zr, and $^{100}$Mo, on the other hand, the values of the nuclear matrix element, like those of the overlap, depend significantly on the EDF. Although such matrix elements

may provide an additional constraint on the pnEDF, the disagreement also suggests, as we noted earlier, that correlations that escape the QRPA are important [38, 39]. Table IX in Appendix B contains more detail than Fig. 4, in particular the values for each individual EDF of all the matrix elements.

In some nuclei, such as $^{76}$Ge, the EDFs all produce comparable values for the matrix element, but those values are quite different from the experimental one. The reason for the discrepancy, again, is the quite different degrees of deformation in the initial and final nuclei, a difference that in reality is probably made less significant by shape fluctuations. In other nuclei, $^{96}$Zr, $^{100}$Mo, and $^{128}$Te (and especially the first two), the values span a wide range. The reason is that two local minima appear in the initial isotopes, and the value of the $2\nu\beta\beta$ matrix element depends strongly on which minimum is used. In these two cases, the HFB overlaps associated with the lowest minima for SkO′ are very small (0.087 and $2.6\times10^{-5}$ in $^{96}$Zr and $^{100}$Mo), and the $2\nu\beta\beta$ matrix elements from the lowest minimum are consequently smaller than the experimental values, while the matrix elements associated with the other HFB solutions are larger than or comparable to the experimental values. Correlations that admix states near those other minima, if they were taken into account, would probably increase the $2\nu\beta\beta$ matrix elements produced by the lowest minima. Such admixtures are beyond what the QRPA includes, however, and seeing their effects would require an approximation such as the generator-coordinate method.

Figure 4 also shows that overlaps computed with the QTDA prescription result in larger matrix elements than those computed with the QRPA prescription.

## B. Predictions

Using the same global EDFs as in the previous section, we compute the $2\nu\beta\beta$ matrix elements for all the nuclei in which that decay might conceivably be observed: $^{46}$Ca, $^{70}$Zn, $^{80}$Se, $^{86}$Kr, $^{94}$Zr, $^{98}$Mo, $^{104}$Ru, $^{110}$Pd, $^{114}$Cd, $^{122}$Sn, $^{124}$Sn, $^{134}$Xe, $^{142}$Ce, $^{146}$Nd, $^{148}$Nd, $^{154}$Sm, $^{160}$Gd, $^{170}$Er, $^{176}$Yb, $^{186}$W, $^{192}$Os, $^{198}$Pt, $^{204}$Hg, $^{226}$Ra, $^{232}$Th, $^{244}$Pu, and $^{248}$Cm. Figure 5 summarizes the results while Table X in Appendix B indicates the individual EDFs responsible for each symbol in the figure. We emphasize that we are able to make these predictions only because we use EDFs that are fit globally and without considering $2\nu\beta\beta$ half-lives. In typical QRPA calculations, by contrast, the strength of isoscalar pairing is adjusted in each nucleus individually to reproduce the $2\nu\beta\beta$ half life.

As we mentioned in the previous subsection, the QRPA nuclear matrix elements may not be reliable if the deformations of the initial and final states of the decay are different. The deformation parameters differ by more than 0.1 for the following decays: $^{70}$Zn → $^{70}$Ge, $^{80}$Se → $^{80}$Kr, $^{134}$Xe → $^{134}$Ba, and $^{146}$Nd → $^{146}$Sm with SkO′ and $^{80}$Se → $^{80}$Kr, $^{114}$Cd → $^{114}$Sn, $^{122}$Sn → $^{122}$Te, $^{134}$Xe → $^{134}$Ba,
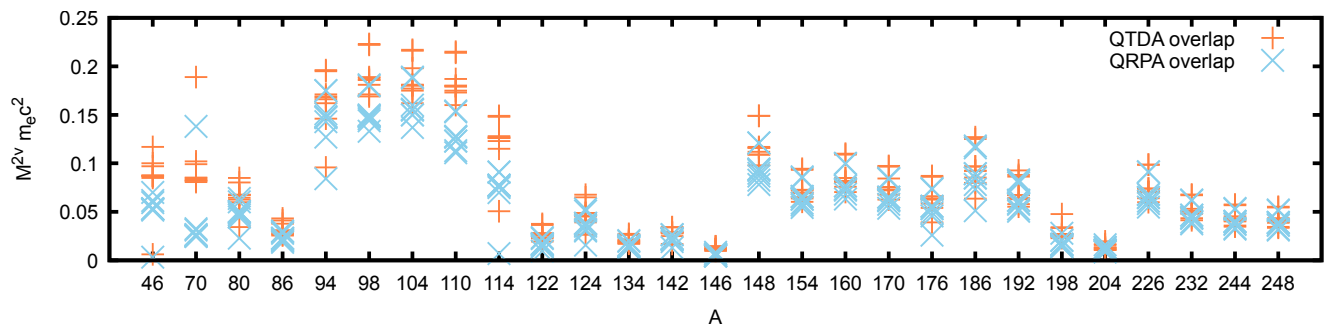
FIG. 5. Dimensionless $2\nu\beta\beta$ nuclear matrix elements calculated with the global EDFs. The matrix elements from parameter set 4 are excluded.

and $^{146}\text{Nd} \rightarrow {}^{146}\text{Sm}$ with SV-min. We also saw earlier that the QRPA can go awry if shape mixing is important. A full treatment of shape mixing requires something like the generator coordinate method [40, 41], but we can get a good idea of when it will be significant by examining potential energy curves. These turn out to be broad near the minimum for the nuclei $^{46}\text{Ti}$, $^{70}\text{Ge}$, $^{94}\text{Zr}$ (only SkO′), $^{98}\text{Mo}$, $^{104}\text{Ru}$, $^{110}\text{Pd}$, $^{114}\text{Cd}$, $^{122}\text{Te}$, $^{124}\text{Te}$, $^{134}\text{Ba}$, $^{142}\text{Ce}$, $^{198}\text{Pt}$, and $^{198}\text{Hg}$. Unfortunately, the generator coordinate method, while it has been applied to $0\nu\beta\beta$ decay [37, 38, 42–52] is difficult to apply to $2\nu\beta\beta$ decay because the closure approximation is poor there and a complete set of intermediate states is required.

With the parameter set 4, the pnFAM converges more slowly than with the other parameter sets, and the resulting matrix elements are often quite different from those produced by the other sets. Thus, we exclude set 4 from the distribution of the nuclear matrix elements shown in Fig. 5. We see better agreement among the other EDFs in heavier isotopes as a general rule, and the QTDA prescription for the overlap again leads to larger numbers than does QRPA prescription.

## VI. CONCLUSIONS

We have presented a computationally efficient framework for calculating the matrix elements for two-neutrino double-beta decay within nuclear density functional theory. We employ the finite amplitude method to compute the QRPA approximation to the matrix elements. Our approach allows large single-particle model spaces and the use of a single nuclear EDF for all nuclei. It also eliminates the need to truncate two-quasiparticle spaces.

We first used harmonic-oscillator based HFB and FAM codes together with familiar EDFs to compute the $2\nu\beta\beta$ matrix elements in a few important nuclei, comparing the results with those obtained previously by diagonalizing the QRPA matrix. Using EDFs that had been fit globally to single-$\beta$ decay rates and giant-resonance energies, we then computed the $2\nu\beta\beta$ matrix elements in all nuclei in which double-beta decay has or could be observed. Agreement with the matrix elements extracted from already measured half-lives is good in general, and we offered predictions for those nuclei that have unmeasured half-lives.

Although we focus on $2\nu\beta\beta$ decay in this paper, we can also compute double-electron capture matrix elements in the same way. The most interesting extension of our work is to neutrinoless double-beta decay. The presence of a neutrino propagator in that matrix element, however,

will make that process more challenging to treat than $2\nu\beta\beta$ decay.

## Appendix A: Overlap

### 1. QRPA overlap

We follow the discussion in Ref. [25] to evaluate the overlap $\langle \lambda_f, K | \lambda_i, K \rangle$ of two intermediate states. The QRPA phonon operators that excite the initial HFB state are related to the those that excite the final state by

$$\hat{\mathcal{Q}}_K^{\lambda_i \dagger} = \sum_{\lambda_f} \left( a_{\lambda_i \lambda_f} \hat{\mathcal{Q}}_K^{\lambda_f \dagger} + b_{\lambda_i \lambda_f} \hat{\tilde{\mathcal{Q}}}_K^{\lambda_f} \right), \qquad (A1)$$

where $\hat{\tilde{\mathcal{Q}}}_K^{\lambda} = \hat{\mathcal{Q}}_{-K}^{\lambda}$. This relation is based on the fact that the both operators span the complete set of two-quasiparticle states with angular momentum projection $K$. The overlap of the intermediate state can be written in terms of the phonon operators as

$$
\begin{aligned}
\langle \lambda_f, K | \lambda_i, K \rangle &= \langle 0_{f,\text{QRPA}}^+ | \hat{\mathcal{Q}}_K^{\lambda_f} \hat{\mathcal{Q}}_K^{\lambda_i \dagger} | 0_{i,\text{QRPA}}^+ \rangle \\
&= \sum_{\lambda_f'} \Big( \langle 0_{f,\text{QRPA}}^+ | \hat{\mathcal{Q}}_K^{\lambda_f} \hat{\mathcal{Q}}_K^{\lambda_f' \dagger} | 0_{i,\text{QRPA}}^+ \rangle a_{\lambda_i \lambda_f'} \\
&\quad + \langle 0_{f,\text{QRPA}}^+ | \hat{\mathcal{Q}}_K^{\lambda_f} \hat{\mathcal{Q}}_{-K}^{\lambda_f'} | 0_{i,\text{QRPA}}^+ \rangle b_{\lambda_i \lambda_f'} \Big) \\
&\approx a_{\lambda_i \lambda_f} \langle 0_{f,\text{HFB}}^+ | 0_{i,\text{HFB}}^+ \rangle, \qquad (A2)
\end{aligned}
$$

where we neglect the term proportional to $b_{\lambda_i \lambda_f'}$, because it involves a two phonon state, and approximate the overlap between the two QRPA correlated ground states.

We have two sets of the quasiparticles, one defined for the initial HFB state and the other for the final state:

$$\hat{a}_\mu^{(i)} | 0_{i,\text{HFB}}^+ \rangle = 0, \quad \hat{a}_\mu^{(f)} | 0_{f,\text{HFB}}^+ \rangle = 0, \qquad (A3)$$

with $\mu$ a proton or neutron single-particle state with positive angular momentum $j_z$ along the symmetry axis.

We write the transformation between the two sets of the quasiparticles in the form

$$\hat{a}_\mu^{(i)\dagger} = \sideset{}{'}\sum_{\nu \in \tau} \left( \mathcal{R}_{\mu\nu} \hat{a}_\nu^{(f)\dagger} + \mathcal{S}_{\mu\bar{\nu}} \hat{a}_{\bar{\nu}}^{(f)} \right), \qquad (A4)$$

$$\hat{a}_{\bar{\mu}}^{(i)\dagger} = \sideset{}{'}\sum_{\nu \in \tau} \left( \mathcal{R}_{\bar{\mu}\bar{\nu}} \hat{a}_{\bar{\nu}}^{(f)\dagger} + \mathcal{S}_{\bar{\mu}\nu} \hat{a}_\nu^{(f)} \right), \qquad (A5)$$

where $\sum'$ means that the summation is only over states with $j_z > 0$, and the notation $\nu \in \tau$ means that index $\nu$ corresponds to the same kind of particle (proton or neutron) as does the index $\mu$ on the left side of the equation.

The relation

$$\mathcal{R}^T \mathcal{R}^* + \mathcal{S}^\dagger \mathcal{S} = I, \qquad (A6)$$

$$\mathcal{R}^T \mathcal{S}^* + \mathcal{S}^\dagger \mathcal{R} = 0 \qquad (A7)$$

follows from the unitarity of the transformation.

This transformation is defined in the full quasiparticle model space; any quasiparticle cutoff thus breaks unitarity. Because the matrix composed of $\mathcal{R}$ and $\mathcal{S}$ is also unitary, the inverse transformation is given by

$$\hat{a}_\mu^{(f)\dagger} = \sideset{}{'}\sum_{\nu \in \tau} \left( \mathcal{S}_{\bar{\nu}\mu} \hat{a}_{\bar{\nu}}^{(i)} + \mathcal{R}_{\nu\mu}^* \hat{a}_\nu^{(i)\dagger} \right), \qquad (A8)$$

$$\hat{a}_{\bar{\mu}}^{(f)\dagger} = \sideset{}{'}\sum_{\nu \in \tau} \left( \mathcal{S}_{\nu\bar{\mu}} \hat{a}_\nu^{(i)} + \mathcal{R}_{\bar{\nu}\bar{\mu}}^* \hat{a}_{\bar{\nu}}^{(i)\dagger} \right). \qquad (A9)$$

Using the Bogoliubov transformation

$$\hat{a}_\mu^{(i/f)\dagger} = \sideset{}{'}\sum_{k \in \tau} V_{\bar{k}\mu}^{(i/f)} \hat{c}_{\bar{k}} + U_{k\mu}^{(i/f)} \hat{c}_k^\dagger, \qquad (A10)$$

$$\hat{a}_{\bar{\mu}}^{(i/f)\dagger} = \sideset{}{'}\sum_{k \in \tau} V_{k\bar{\mu}}^{(i/f)} \hat{c}_k + U_{\bar{k}\bar{\mu}}^{(i/f)} \hat{c}_{\bar{k}}^\dagger, \qquad (A11)$$

we can write the matrix elements of $\mathcal{R}$ and $\mathcal{S}$ in the form

$$\mathcal{R}_{\mu\nu} = \sideset{}{'}\sum_{k \in \tau} V_{\bar{k}\mu}^{(i)} V_{\bar{k}\nu}^{(f)*} + U_{k\mu}^{(i)} U_{k\nu}^{(f)*}, \qquad (A12)$$

$$\mathcal{R}_{\bar{\mu}\bar{\nu}} = \sideset{}{'}\sum_{k \in \tau} V_{k\bar{\mu}}^{(i)} V_{k\bar{\nu}}^{(f)*} + U_{\bar{k}\bar{\mu}}^{(i)} U_{\bar{k}\bar{\nu}}^{(f)*}, \qquad (A13)$$

$$\mathcal{S}_{\mu\bar{\nu}} = \sideset{}{'}\sum_{k \in \tau} V_{\bar{k}\mu}^{(i)} U_{\bar{k}\bar{\nu}}^{(f)} + U_{k\mu}^{(i)} V_{k\bar{\nu}}^{(f)}, \qquad (A14)$$

$$\mathcal{S}_{\bar{\mu}\nu} = \sideset{}{'}\sum_{k \in \tau} V_{k\bar{\mu}}^{(i)} U_{k\nu}^{(f)} + U_{\bar{k}\bar{\mu}}^{(i)} V_{\bar{k}\nu}^{(f)}. \qquad (A15)$$

Defining the proton-neutron two-quasiparticle creation and annihilation operators

$$\boldsymbol{A}^{(i)\dagger}(pn, K) \equiv \hat{a}_p^{(i)\dagger} \hat{a}_n^{(i)\dagger}, \quad \boldsymbol{A}^{(i)\dagger}(\bar{p}\bar{n}, K) \equiv \hat{a}_{\bar{p}}^{(i)\dagger} \hat{a}_{\bar{n}}^{(i)\dagger}, \qquad (A16)$$

we can relate the two-quasiparticle operators defined with respect to the initial and final HFB states in the

following way:

$$\boldsymbol{A}^{(i)\dagger}(pn,K) = \sum_{p'n'}' \left[ \mathcal{R}_{pp'}\mathcal{R}_{nn'}\boldsymbol{A}^{(f)\dagger}(p'n',K) \right.$$
$$\left. - \mathcal{S}_{p\bar{p}'}\mathcal{S}_{n\bar{n}'}\boldsymbol{A}^{(f)}(\bar{p}'\bar{n}',K) \right] + (\hat{a}^\dagger\hat{a}-\text{terms}),$$
(A17)

$$\boldsymbol{A}^{(i)}(\bar{p}\bar{n},K) = \sum_{p'n'}' \left[ \mathcal{R}^*_{\bar{p}\bar{p}'}\mathcal{R}^*_{\bar{n}\bar{n}'}\boldsymbol{A}^{(f)}(\bar{p}'\bar{n}',K) \right.$$
$$\left. - \mathcal{S}^*_{\bar{p}p'}\mathcal{S}^*_{\bar{n}n'}\boldsymbol{A}^{(f)\dagger}(p'n',K) \right] + (\hat{a}^\dagger\hat{a}-\text{terms}).$$
(A18)

The QRPA phonon operator is a combination of two-quasiparticle creation and annihilation operators:

$$\hat{\mathcal{Q}}^{\lambda_i\dagger}_K = \sum_{pn}' \left[ X^{\lambda_i}_{pn,K}\boldsymbol{A}^{(i)\dagger}(pn,K) - Y^{\lambda_i}_{pn,K}\boldsymbol{A}^{(i)}(\bar{p}\bar{n},K) \right],$$
(A19)

$$\hat{\bar{\mathcal{Q}}}^{\lambda_i}_K = \sum_{pn}' \left[ X^{\lambda_i}_{pn,K}\boldsymbol{A}^{(i)}(\bar{p}\bar{n},K) - Y^{\lambda_i}_{pn,K}\boldsymbol{A}^{(i)\dagger}(pn,K) \right].$$
(A20)

Inverting this yields the relation

$$\boldsymbol{A}^{(f)\dagger}(pn,K) = \sum_{\lambda_f} \left[ X^{\lambda_f*}_{pn,K}\hat{\mathcal{Q}}^{\lambda_f\dagger}_K + Y^{\lambda_f*}_{pn,K}\hat{\bar{\mathcal{Q}}}^{\lambda_f}_K \right], \quad (A21)$$

$$\boldsymbol{A}^{(f)}(\bar{p}\bar{n},K) = \sum_{\lambda_f} \left[ X^{\lambda_f*}_{pn,K}\hat{\bar{\mathcal{Q}}}^{\lambda_f}_K + Y^{\lambda_f*}_{pn,K}\hat{\mathcal{Q}}^{\lambda_f\dagger}_K \right], \quad (A22)$$

which leads to an expression for the $a$ matrix in Eq. (A2):

$$a_{\lambda_i\lambda_f} = \sum_{pnp'n'}' \left[ X^{\lambda_f*}_{p'n',K}\mathcal{R}_{pp'}\mathcal{R}_{nn'}X^{\lambda_i}_{pn,K} \right.$$
$$- Y^{\lambda_f*}_{p'n',K}\mathcal{R}^*_{\bar{p}\bar{p}'}\mathcal{R}^*_{\bar{n}\bar{n}'}Y^{\lambda_i}_{pn,K}$$
$$+ X^{\lambda_f*}_{p'n',K}\mathcal{S}^*_{\bar{p}p'}\mathcal{S}^*_{\bar{n}n'}Y^{\lambda_i}_{pn,K}$$
$$\left. - Y^{\lambda_f*}_{p'n',K}\mathcal{S}_{p\bar{p}'}\mathcal{S}_{n\bar{n}'}X^{\lambda_i}_{pn,K} \right].$$
(A23)

In Ref. [25], the contribution from $\mathcal{S}$ in Eq. (A23) is neglected.

The overlap between the HFB states is given by the Onishi formula, e.g. in Eq. (E.49) of Ref. [40]:

$$\mathcal{N}^{-1} = \langle 0^+_{f,\text{HFB}}|0^+_{i,\text{HFB}}\rangle = \langle 0^+_{i,\text{HFB}}|0^+_{f,\text{HFB}}\rangle$$
$$= \left( \det \mathcal{R}^T \right)^{\frac{1}{2}} = \left[ \det \left( 1 + \mathcal{D}^\dagger\mathcal{D} \right) \right]^{-\frac{1}{4}}, \quad (A24)$$

where $\mathcal{D}$ is a skew-symmetric matrix that determines the relation between the initial and final HFB states through

$$|0^+_{i,\text{HFB}}\rangle = \mathcal{N}^{-1} \exp \left( \sum_\tau \sum_{\mu\nu\in\tau} \mathcal{D}_{\mu\nu}\hat{a}^{(f)\dagger}_\mu\hat{a}^{(f)\dagger}_\nu \right) |0^+_{f,\text{HFB}}\rangle,$$
(A25)

and satisfies the relation

$$\mathcal{D} = \mathcal{S}^\dagger(\mathcal{R}^\dagger)^{-1} = -(\mathcal{R}^{-1}\mathcal{S})^* = -\mathcal{D}^T. \quad (A26)$$

Thus, we end up with

$$\langle \lambda_f, K|\lambda_i, K\rangle = (\det \mathcal{R})^{\frac{1}{2}} \sum_{pnp'n'}' \mathcal{R}_{pp'}\mathcal{R}_{nn'}$$
$$\times \left( X^{\lambda_f*}_{p'n',K}X^{\lambda_i}_{pn,K} - Y^{\lambda_f*}_{p'n',K}Y^{\lambda_i}_{pn,K} \right).$$
(A27)

### 2. QTDA overlap

Reference [8] uses the QTDA to evaluate the overlap among intermediate states, which are given by

$$|\lambda_{i/f}, K\rangle = \sum_{pn} X^{\lambda_{i/f}}_{\mu\nu,K}\hat{a}^{(i/f)\dagger}_p\hat{a}^{(i/f)\dagger}_n|0^+_{i/f,\text{HFB}}\rangle. \quad (A28)$$

From Eqs. (A25) and (A28), we find that

$$\langle \lambda_f, K|\lambda_i, K\rangle = (\det \mathcal{R})^{\frac{1}{2}} \sum_{pnp'n'}' X^{\lambda_f*}_{p'n',K}X^{\lambda_i}_{pn,K}$$
$$\times \left( \mathcal{R}_{pp'} + 2\sum_{p''}\mathcal{S}_{pp''}\mathcal{D}_{p''p'} \right)$$
$$\times \left( \mathcal{R}_{nn'} + 2\sum_{n''}\mathcal{S}_{nn''}\mathcal{D}_{n''n'} \right). \quad (A29)$$

The two QRPA and QTDA overlaps in Eqs. (A27) and (A29) can be written in the same form as

$$\langle \lambda_f, K|\lambda_i, K\rangle = \sum_{pnp'n'}' \left( X^{\lambda_f*}_{p'n',K}X^{\lambda_i}_{pn,K} - \alpha Y^{\lambda_f*}_{p'n',K}Y^{\lambda_i}_{pn,K} \right)$$
$$\times \mathcal{O}_{pp'}(\alpha)\mathcal{O}_{nn'}(\alpha), \quad (A30)$$

where $\mathcal{O}$ is a matrix that does not depend on the QRPA and includes the HFB overlap and the transformation relating the initial and final quasiparticle states

$$\mathcal{O}_{\rho\rho'}(\alpha) = \left[ \det \mathcal{R}^{(\tau)} \right]^{\frac{1}{2}} \left[ \mathcal{R}_{\rho\rho'} + 2(1-\alpha)\sum_{\rho''\in\tau}'\mathcal{S}_{\rho\rho''}\mathcal{D}_{\rho''\rho'} \right].$$
(A31)

Here $\rho, \rho'$ are both proton or both neutron states, and $\mathcal{R}^{(\tau)}$ is the neutron or proton part of the matrix $\mathcal{R}$. The QRPA expression in Ref. [25] corresponds $\alpha = 1$ and the QTDA expression in Ref. [8] to $\alpha = 0$.

### Appendix B: Numerical Results for Matrix Elements in Individual Nuclei

Table IX below provides details related to Fig. 4. Table X does the same for Fig. 5.

TABLE IX. Dimensionless Gamow-Teller $2\nu\beta\beta$ nuclear matrix element $m_e c^2 M_{\mathrm{GT}}^{2\nu}$ computed with the SkO'- and SV-min-based EDFs, with globally fitted proton-neutron parts [15]. The value of the matrix element is compared with experimental values extracted from Ref. [5]. The overlap of the intermediate states is evaluated both with QTDA ($\alpha = 0$, Ref. [8]) and QRPA ($\alpha = 1$, Ref. [25]) prescriptions. The numbers in parentheses denote powers of 10.

| | $\alpha$ | 1A | 1B | 1C | 1D | 1E | 2 | 3A | 3B | 4 | 5 | Exp. |
|---|---|---|---|---|---|---|---|---|---|---|---|---|
| $^{48}$Ca | 0 | 0.0759 | 0.0734 | 0.0763 | 0.0722 | 0.0934 | 0.0698 | 0.0729 | 0.0879 | 0.0706 | 0.118 | 0.035±0.003 |
| | 1 | 0.0399 | 0.0386 | 0.0401 | 0.0382 | 0.0489 | 0.0372 | 0.0386 | 0.0463 | 0.0385 | 0.0588 | |
| $^{76}$Ge | 0 | 0.0496 | 0.0477 | 0.0496 | 0.0441 | 0.062 | 0.0469 | 0.0462 | 0.0588 | 0.0502 | 0.0426 | 0.106± 0.004 |
| | 1 | 0.0343 | 0.033 | 0.0344 | 0.0304 | 0.0431 | 0.0331 | 0.0319 | 0.0409 | 0.0355 | 0.0293 | |
| $^{82}$Se | 0 | 0.0572 | 0.0547 | 0.0572 | 0.05 | 0.0736 | 0.0543 | 0.0528 | 0.0693 | 0.0567 | 0.061 | 0.085± 0.001 |
| | 1 | 0.0464 | 0.0444 | 0.0464 | 0.0404 | 0.0599 | 0.0463 | 0.0428 | 0.0564 | 0.0474 | 0.0485 | |
| $^{96}$Zr | 0 | 0.0265 | 0.0257 | 0.0267 | 0.026 | 0.0321 | 0.123 | 0.0267 | 0.032 | 0.0296 | 0.0228 | 0.080±0.004 |
| | 1 | 0.0133 | 0.0129 | 0.0134 | 0.013 | 0.0164 | 0.108 | 0.0134 | 0.0164 | 0.015 | 0.0113 | |
| ($^{96}$Zr sph.) | 0 | 0.202 | 0.197 | 0.204 | 0.202 | 0.243 | 0.123 | 0.207 | 0.244 | 0.232 | 0.173 | |
| | 1 | 0.18 | 0.175 | 0.181 | 0.178 | 0.219 | 0.108 | 0.183 | 0.22 | 0.206 | 0.152 | |
| $^{100}$Mo | 0 | 1.71(−5) | 1.67(−5) | 1.72(−5) | 1.69(−5) | 2.02(−5) | 0.234 | 1.73(−5) | 2.01(−5) | 1.7(−5) | 1.53(−5) | 0.151± 0.005 |
| | 1 | 2.67(−6) | 2.58(−6) | 2.68(−6) | 2.57(−6) | 3.25(−6) | 0.2 | 2.67(−6) | 3.24(−6) | 3.16(−6) | 2.32(−6) | |
| ($^{100}$Mo pro.) | 0 | 0.166 | 0.161 | 0.167 | 0.162 | 0.201 | 0.234 | 0.166 | 0.199 | 0.179 | 0.147 | |
| | 1 | 0.142 | 0.138 | 0.143 | 0.137 | 0.175 | 0.2 | 0.142 | 0.173 | 0.16 | 0.125 | |
| $^{116}$Cd | 0 | 0.11 | 0.107 | 0.111 | 0.108 | 0.131 | 0.0606 | 0.11 | 0.13 | 0.082 | 0.0997 | 0.108±0.003 |
| | 1 | 0.0728 | 0.0708 | 0.0732 | 0.0707 | 0.0865 | 0.0132 | 0.0725 | 0.086 | 0.0541 | 0.0655 | |
| $^{128}$Te | 0 | 0.0161 | 0.0153 | 0.0161 | 0.0137 | 0.0215 | 0.0124 | 0.0149 | 0.0207 | 0.00873 | 0.0131 | 0.043±0.003 |
| | 1 | 0.00993 | 0.00944 | 0.00994 | 0.00848 | 0.0134 | 0.00695 | 0.00923 | 0.0129 | 0.00626 | 0.00808 | |
| ($^{128}$Xe obl.) | 0 | 0.0306 | 0.0291 | 0.0306 | 0.0263 | 0.0407 | 0.0263 | 0.0285 | 0.0393 | 0.0155 | 0.0251 | |
| | 1 | 0.0195 | 0.0185 | 0.0195 | 0.0165 | 0.0264 | 0.0154 | 0.018 | 0.0253 | 0.0106 | 0.0159 | |
| $^{130}$Te | 0 | 0.0227 | 0.0215 | 0.0227 | 0.0189 | 0.0308 | 0.0215 | 0.0208 | 0.0295 | 0.0149 | 0.0185 | 0.0293±0.0009 |
| | 1 | 0.0168 | 0.0159 | 0.0168 | 0.0141 | 0.0229 | 0.0151 | 0.0154 | 0.0219 | 0.0118 | 0.0138 | |
| $^{136}$Xe | 0 | 0.0222 | 0.0208 | 0.0221 | 0.0173 | 0.0318 | 0.0238 | 0.0194 | 0.0296 | 0.0184 | 0.0232 | 0.0181± 0.0006 |
| | 1 | 0.018 | 0.0169 | 0.018 | 0.0139 | 0.0261 | 0.0201 | 0.0156 | 0.0243 | 0.0136 | 0.0175 | |
| $^{150}$Nd | 0 | 0.0413 | 0.0395 | 0.0414 | 0.0369 | 0.0541 | 0.0552 | 0.0399 | 0.0536 | 0.0511 | 0.0341 | 0.044 ± 0.005 |
| | 1 | 0.0345 | 0.0329 | 0.0346 | 0.0308 | 0.0455 | 0.0463 | 0.0334 | 0.0451 | 0.0425 | 0.0284 | |
| $^{238}$U | 0 | 0.0462 | 0.044 | 0.0462 | 0.039 | 0.0616 | 0.048 | 0.0434 | 0.0609 | 0.0717 | 0.0374 | $0.13^{+0.09}_{-0.07}$ |
| | 1 | 0.0428 | 0.0407 | 0.0428 | 0.0359 | 0.0573 | 0.0431 | 0.04 | 0.0566 | 0.0597 | 0.0345 | |

[1] F. T. Avignone, S. R. Elliott, and J. Engel, Double beta decay, Majorana neutrinos, and neutrino mass, Rev. Mod. Phys. **80**, 481 (2008).

[2] J. Engel and J. Menéndez, Status and future of nuclear matrix elements for neutrinoless double-beta decay: a review, Rep. Prog. Phys. **80**, 046301 (2017).

[3] H. Ejiri, J. Suhonen, and K. Zuber, Neutrino–nuclear responses for astro-neutrinos, single beta decays and double beta decays, Phys. Rep. **797**, 1 (2019).

[4] H. Ejiri, Neutrino-mass sensitivity and nuclear matrix element for neutrinoless double beta decay, Universe **6**, 225 (2020).

[5] A. Barabash, Precise half-life values for two-neutrino double-$\beta$ decay: 2020 review, Universe **6**, 159 (2020).

[6] P. Vogel and M. R. Zirnbauer, Suppression of the two-neutrino double-beta decay by nuclear-structure effects, Phys. Rev. Lett. **57**, 3148 (1986).

[7] J. Engel, P. Vogel, and M. R. Zirnbauer, Nuclear structure effects in double-beta decay, Phys. Rev. C **37**, 731 (1988).

[8] M. T. Mustonen and J. Engel, Large-scale calculations of the double-beta decay of $^{76}$Ge, $^{130}$Te, $^{136}$Xe, and $^{150}$Nd in the deformed self-consistent Skyrme quasipar-ticle random-phase approximation, Phys. Rev. C **87**, 064302 (2013).

[9] S. Bogner, A. Bulgac, J. Carlson, J. Engel, G. Fann, R. Furnstahl, S. Gandolfi, G. Hagen, M. Horoi, C. Johnson, M. Kortelainen, E. Lusk, P. Maris, H. Nam, P. Navratil, W. Nazarewicz, E. Ng, G. Nobre, E. Ormand, T. Papenbrock, J. Pei, S. Pieper, S. Quaglioni, K. Roche, J. Sarich, N. Schunck, M. Sosonkina, J. Terasaki, I. Thompson, J. Vary, and S. Wild, Computational nuclear quantum many-body problem: The UNEDF project, Comput. Phys. Commun. **184**, 2235 (2013).

[10] M. Kortelainen, T. Lesinski, J. Moré, W. Nazarewicz, J. Sarich, N. Schunck, M. V. Stoitsov, and S. Wild, Nuclear energy density optimization, Phys. Rev. C **82**, 024313 (2010).

[11] M. Kortelainen, J. McDonnell, W. Nazarewicz, P.-G. Reinhard, J. Sarich, N. Schunck, M. V. Stoitsov, and S. M. Wild, Nuclear energy density optimization: Large deformations, Phys. Rev. C **85**, 024304 (2012).

[12] M. Kortelainen, J. McDonnell, W. Nazarewicz, E. Olsen, P.-G. Reinhard, J. Sarich, N. Schunck, S. M. Wild, D. Davesne, J. Erler, and A. Pastore, Nuclear energy

TABLE X. Dimensionless Gamow-Teller $2\nu\beta\beta$ nuclear matrix element $m_e c^2 M_{\mathrm{GT}}^{2\nu}$ for nuclei whose half lives have not been measured yet. The column and row labels are the same as in Table IX.

| | $\alpha$ | 1A | 1B | 1C | 1D | 1E | 2 | 3A | 3B | 4 | 5 |
|---|---|---|---|---|---|---|---|---|---|---|---|
| $^{46}$Ca | 0 | 0.0868 | 0.0849 | 0.0874 | 0.0874 | 0.1 | 0.00611 | 0.0867 | 0.097 | 0.0831 | 0.117 |
| | 1 | 0.0529 | 0.0518 | 0.0534 | 0.0532 | 0.0616 | 0.00332 | 0.0529 | 0.0595 | 0.0534 | 0.07 |
| $^{70}$Zn | 0 | 0.0848 | 0.0823 | 0.0854 | 0.0823 | 0.102 | 0.189 | 0.0831 | 0.0992 | 0.0982 | 0.0807 |
| | 1 | 0.0263 | 0.0254 | 0.0265 | 0.0248 | 0.0326 | 0.138 | 0.0252 | 0.0312 | 0.0306 | 0.0246 |
| $^{80}$Se | 0 | 0.0673 | 0.0646 | 0.0674 | 0.0599 | 0.0849 | 0.0343 | 0.0626 | 0.0802 | 0.0657 | 0.0677 |
| | 1 | 0.0505 | 0.0485 | 0.0505 | 0.0446 | 0.0638 | 0.0228 | 0.0468 | 0.0603 | 0.0507 | 0.0495 |
| $^{86}$Kr | 0 | 0.0308 | 0.0293 | 0.0308 | 0.0256 | 0.0411 | 0.0267 | 0.0274 | 0.0379 | 0.0276 | 0.0433 |
| | 1 | 0.0228 | 0.0217 | 0.0227 | 0.0187 | 0.0303 | 0.0208 | 0.0201 | 0.028 | 0.0206 | 0.0294 |
| $^{94}$Zr | 0 | 0.166 | 0.162 | 0.168 | 0.169 | 0.195 | 0.0959 | 0.171 | 0.196 | 0.195 | 0.146 |
| | 1 | 0.147 | 0.143 | 0.148 | 0.148 | 0.175 | 0.0841 | 0.151 | 0.175 | 0.172 | 0.127 |
| $^{98}$Mo | 0 | 0.186 | 0.181 | 0.188 | 0.186 | 0.223 | 0.171 | 0.189 | 0.222 | 0.208 | 0.169 |
| | 1 | 0.149 | 0.144 | 0.15 | 0.146 | 0.181 | 0.148 | 0.149 | 0.18 | 0.168 | 0.133 |
| $^{104}$Ru | 0 | 0.18 | 0.175 | 0.181 | 0.177 | 0.217 | 0.198 | 0.181 | 0.216 | −0.718 | 0.162 |
| | 1 | 0.155 | 0.15 | 0.156 | 0.15 | 0.189 | 0.16 | 0.155 | 0.188 | −0.149 | 0.137 |
| $^{110}$Pd | 0 | 0.179 | 0.173 | 0.18 | 0.175 | 0.215 | 0.187 | 0.18 | 0.214 | 0.279 | 0.16 |
| | 1 | 0.127 | 0.123 | 0.128 | 0.123 | 0.154 | 0.111 | 0.127 | 0.153 | 0.134 | 0.113 |
| $^{114}$Cd | 0 | 0.126 | 0.123 | 0.127 | 0.126 | 0.149 | 0.0506 | 0.128 | 0.148 | 0.102 | 0.115 |
| | 1 | 0.0771 | 0.0751 | 0.0776 | 0.0762 | 0.0911 | 0.00702 | 0.0775 | 0.0908 | 0.0623 | 0.0699 |
| $^{122}$Sn | 0 | 0.0279 | 0.0265 | 0.028 | 0.0239 | 0.0377 | 0.0193 | 0.026 | 0.0364 | 0.0645 | 0.0226 |
| | 1 | 0.0171 | 0.0162 | 0.0172 | 0.0145 | 0.0234 | 0.00955 | 0.0159 | 0.0225 | 0.0285 | 0.0137 |
| $^{124}$Sn | 0 | 0.0488 | 0.0462 | 0.0489 | 0.041 | 0.0676 | 0.0263 | 0.0451 | 0.065 | 0.055 | 0.0391 |
| | 1 | 0.0382 | 0.0361 | 0.0382 | 0.0319 | 0.053 | 0.0157 | 0.0351 | 0.0508 | 0.0386 | 0.0303 |
| $^{134}$Xe | 0 | 0.0203 | 0.0192 | 0.0202 | 0.017 | 0.0274 | 0.0218 | 0.0185 | 0.0261 | 0.0142 | 0.0176 |
| | 1 | 0.015 | 0.0142 | 0.015 | 0.0126 | 0.0204 | 0.016 | 0.0138 | 0.0195 | 0.0114 | 0.0131 |
| $^{142}$Ce | 0 | 0.0289 | 0.0281 | 0.029 | 0.0277 | 0.0339 | 0.0168 | 0.0291 | 0.0343 | 0.0322 | 0.025 |
| | 1 | 0.0224 | 0.0218 | 0.0225 | 0.0215 | 0.0264 | 0.013 | 0.0226 | 0.0266 | 0.026 | 0.0194 |
| $^{146}$Nd | 0 | 0.0117 | 0.0113 | 0.0117 | 0.0109 | 0.0145 | 0.0135 | 0.0116 | 0.0145 | 0.0145 | 0.00979 |
| | 1 | 0.00512 | 0.00491 | 0.00514 | 0.0047 | 0.00655 | 0.00832 | 0.00505 | 0.00654 | 0.00663 | 0.00419 |
| $^{148}$Nd | 0 | 0.116 | 0.112 | 0.117 | 0.109 | 0.149 | 0.109 | 0.116 | 0.149 | 0.137 | 0.0979 |
| | 1 | 0.0937 | 0.0898 | 0.0942 | 0.0869 | 0.121 | 0.0826 | 0.0928 | 0.121 | 0.112 | 0.0782 |
| $^{154}$Sm | 0 | 0.0725 | 0.0694 | 0.0728 | 0.0652 | 0.0944 | 0.0639 | 0.0701 | 0.0933 | 0.0958 | 0.0603 |
| | 1 | 0.0658 | 0.0629 | 0.066 | 0.0589 | 0.0862 | 0.0571 | 0.0635 | 0.0852 | 0.083 | 0.0545 |
| $^{160}$Gd | 0 | 0.0847 | 0.081 | 0.085 | 0.0759 | 0.11 | 0.0807 | 0.0819 | 0.109 | 0.097 | 0.0704 |
| | 1 | 0.0766 | 0.0732 | 0.0768 | 0.0682 | 0.1 | 0.0724 | 0.0737 | 0.0994 | 0.0914 | 0.0633 |
| $^{170}$Er | 0 | 0.0753 | 0.0722 | 0.0756 | 0.0677 | 0.0974 | 0.0844 | 0.0729 | 0.0965 | −0.0389 | 0.0627 |
| | 1 | 0.0651 | 0.0622 | 0.0652 | 0.0578 | 0.0847 | 0.0612 | 0.0626 | 0.0837 | 0.025 | 0.0538 |
| $^{176}$Yb | 0 | 0.0657 | 0.0627 | 0.0659 | 0.0585 | 0.087 | 0.0391 | 0.0635 | 0.0862 | −0.0577 | 0.0542 |
| | 1 | 0.0557 | 0.0531 | 0.0558 | 0.0493 | 0.074 | 0.026 | 0.0536 | 0.0733 | 0.0181 | 0.0457 |
| $^{186}$W | 0 | 0.0966 | 0.0923 | 0.0969 | 0.0853 | 0.127 | 0.0637 | 0.0923 | 0.125 | −0.07 | 0.0799 |
| | 1 | 0.0892 | 0.0851 | 0.0894 | 0.0781 | 0.118 | 0.0512 | 0.0848 | 0.116 | 0.00665 | 0.0733 |
| $^{192}$Os | 0 | 0.0672 | 0.0642 | 0.0673 | 0.0579 | 0.0881 | 0.0927 | 0.0631 | 0.0863 | −0.0446 | 0.0553 |
| | 1 | 0.0618 | 0.0589 | 0.0618 | 0.0529 | 0.0814 | 0.083 | 0.0578 | 0.0797 | −0.0295 | 0.0506 |
| $^{198}$Pt | 0 | 0.0272 | 0.0262 | 0.0272 | 0.0238 | 0.0341 | 0.0478 | 0.0255 | 0.0333 | 0.396 | 0.0229 |
| | 1 | 0.0167 | 0.016 | 0.0167 | 0.0144 | 0.0209 | 0.0279 | 0.0155 | 0.0204 | −0.0265 | 0.014 |
| $^{204}$Hg | 0 | 0.0133 | 0.0127 | 0.0132 | 0.0107 | 0.0167 | 0.0195 | 0.0117 | 0.016 | −0.023 | 0.0109 |
| | 1 | 0.0108 | 0.0104 | 0.0107 | 0.0087 | 0.0136 | 0.0161 | 0.00954 | 0.013 | 0.0178 | 0.00885 |
| $^{226}$Ra | 0 | 0.0739 | 0.0703 | 0.074 | 0.064 | 0.0987 | 0.0706 | 0.0708 | 0.0986 | 0.343 | 0.06 |
| | 1 | 0.068 | 0.0646 | 0.068 | 0.0585 | 0.0913 | 0.061 | 0.0649 | 0.091 | 0.172 | 0.0549 |
| $^{232}$Th | 0 | 0.0509 | 0.0485 | 0.0509 | 0.0434 | 0.0678 | 0.0531 | 0.0481 | 0.0672 | 0.171 | 0.0414 |
| | 1 | 0.0465 | 0.0443 | 0.0465 | 0.0394 | 0.0623 | 0.0433 | 0.0438 | 0.0617 | 0.0894 | 0.0376 |
| $^{244}$Pu | 0 | 0.0431 | 0.0409 | 0.043 | 0.0359 | 0.0576 | 0.0454 | 0.0401 | 0.0568 | 0.0265 | 0.0347 |
| | 1 | 0.0399 | 0.0379 | 0.0399 | 0.0331 | 0.0536 | 0.0404 | 0.037 | 0.0528 | 0.0384 | 0.0321 |
| $^{248}$Cm | 0 | 0.0415 | 0.0394 | 0.0414 | 0.0346 | 0.0552 | 0.0435 | 0.0387 | 0.0545 | −0.00664 | 0.0335 |
| | 1 | 0.0389 | 0.0369 | 0.0388 | 0.0322 | 0.052 | 0.0391 | 0.0361 | 0.0512 | 0.0184 | 0.0313 |

density optimization: Shell structure, Phys. Rev. C **89**, 054314 (2014).

[13] N. Schunck, J. D. McDonnell, J. Sarich, S. M. Wild, and D. Higdon, Error analysis in nuclear density functional theory, J. Phys. G **42**, 034024 (2015).

[14] P. Klüpfel, P.-G. Reinhard, T. J. Bürvenich, and J. A. Maruhn, Variations on a theme by Skyrme: A systematic study of adjustments of model parameters, Phys. Rev. C **79**, 034310 (2009).

[15] M. T. Mustonen and J. Engel, Global description of $\beta^-$ decay in even-even nuclei with the axially-deformed Skyrme finite-amplitude method, Phys. Rev. C **93**, 014304 (2016).

[16] T. Nakatsukasa, T. Inakura, and K. Yabana, Finite amplitude method for the solution of the random-phase approximation, Phys. Rev. C **76**, 024318 (2007).

[17] P. Avogadro and T. Nakatsukasa, Finite amplitude method for the quasiparticle random-phase approximation, Phys. Rev. C **84**, 014314 (2011).

[18] M. T. Mustonen, T. Shafer, Z. Zenginerler, and J. Engel, Finite-amplitude method for charge-changing transitions in axially deformed nuclei, Phys. Rev. C **90**, 024308 (2014).

[19] T. Shafer, J. Engel, C. Fröhlich, G. C. McLaughlin, M. Mumpower, and R. Surman, $\beta$ decay of deformed r-process nuclei near $a = 80$ and $a = 160$, including odd-$a$ and odd-odd- nuclei, with the Skyrme finite-amplitude method, Phys. Rev. C **94**, 055802 (2016).

[20] E. M. Ney, J. Engel, T. Li, and N. Schunck, Global description of $\beta^-$ decay with the axially deformed Skyrme finite-amplitude method: Extension to odd-mass and odd-odd nuclei, Phys. Rev. C **102**, 034326 (2020).

[21] N. Hinohara, Efficient QRPA calculation for two-neutrino double-beta decay nuclear matrix element, AIP Conf. Proc. **2165**, 020010 (2019).

[22] N. Hinohara, M. Kortelainen, and W. Nazarewicz, Low-energy collective modes of deformed superfluid nuclei within the finite-amplitude method, Phys. Rev. C **87**, 064309 (2013).

[23] N. Hinohara, M. Kortelainen, W. Nazarewicz, and E. Olsen, Complex-energy approach to sum rules within nuclear density functional theory, Phys. Rev. C **91**, 044323 (2015).

[24] F. Šimkovic, V. Rodin, A. Faessler, and P. Vogel, $0\nu\beta\beta$ and $2\nu\beta\beta$ nuclear matrix elements, quasiparticle random-phase approximation, and isospin symmetry restoration, Phys. Rev. C **87**, 045501 (2013).

[25] F. Šimkovic, L. Pacearescu, and A. Faessler, Two-neutrino double beta decay of $^{76}$Ge within deformed QRPA, Nucl. Phys. A **733**, 321 (2004).

[26] R. N. Perez, N. Schunck, R.-D. Lasseri, C. Zhang, and J. Sarich, Axially deformed solution of the Skyrme–Hartree–Bogolyubov equations using the transformed harmonic oscillator basis (iii) HFBTHO (v3.00): A new version of the program, Comput. Phys. Commun. **220**, 363 (2017).

[27] M. V. Stoitsov, N. Schunck, M. Kortelainen, N. Michel, H. Nam, E. Olsen, J. Sarich, and S. Wild, Axially deformed solution of the Skyrme-Hartree-Fock-Bogoliubov equations using the transformed harmonic oscillator basis (ii) HFBTHO v2.00d: A new version of the program, Comput. Phys. Commun. **184**, 1592 (2013).

[28] M. V. Stoitsov, J. Dobaczewski, W. Nazarewicz, and P. Ring, Axially deformed solution of the Skyrme-Hartree-Fock-Bogolyubov equations using the transformed harmonic oscillator basis. the program HFBTHO (v1.66p), Comput. Phys. Commun. **167**, 43 (2005).

[29] M. Wang, W. Huang, F. Kondev, G. Audi, and S. Naimi, The AME 2020 atomic mass evaluation (II). Tables, graphs and references, Chin Phys. C **45**, 030003 (2021).

[30] J. Bartel, P. Quentin, M. Brack, C. Guet, and H.-B. Håkansson, Towards a better parametrisation of Skyrme-like effective forces: A critical study of the SkM force, Nucl. Phys. A **386**, 79 (1982).

[31] M. Bender, K. Rutz, P.-G. Reinhard, and J. Maruhn, Pairing gaps from nuclear mean-field models, Eur. Phys. J. A **8**, 59 (2000).

[32] D.-L. Fang, A. Faessler, V. Rodin, and F. Šimkovic, Neutrinoless double-$\beta$ decay of deformed nuclei within quasiparticle random-phase approximation with a realistic interaction, Phys. Rev. C **83**, 034320 (2011).

[33] D.-L. Fang, A. Faessler, and F. Šimkovic, $0\nu\beta\beta$-decay nuclear matrix element for light and heavy neutrino mass mechanisms from deformed quasiparticle random-phase approximation calculations for $^{76}$Ge,$^{82}$Se,$^{130}$Te,$^{136}$Xe, and $^{150}$Nd with isospin restoration, Phys. Rev. C **97**, 045503 (2018).

[34] P.-G. Reinhard, D. J. Dean, W. Nazarewicz, J. Dobaczewski, J. A. Maruhn, and M. R. Strayer, Shape coexistence and the effective nucleon-nucleon interaction, Phys. Rev. C **60**, 014316 (1999).

[35] M. T. Mustonen, (private communication).

[36] N. L. Vaquero, T. R. Rodriguez, and J. L. Egido, On the impact of large amplitude pairing fluctuations on nuclear spectra, Phys. Lett. B **704**, 520 (2011).

[37] N. Hinohara and J. Engel, Proton-neutron pairing amplitude as a generator coordinate for double-$\beta$ decay, Phys. Rev. C **90**, 031301(R) (2014).

[38] T. R. Rodríguez and G. Martinez-Pinedo, Neutrinoless double beta decay studied with configuration mixing methods, Prog. Part. Nucl. Phys. **66**, 436 (2011).

[39] T. R. Rodríguez, Role of triaxiality in $^{76}$Ge and $^{76}$Se nuclei studied with Gogny energy density functionals, J. Phys. G: Nucl. Part. Phys. **44**, 034002 (2017).

[40] P. Ring and P. Schuck, The Nuclear Many-Body Problem (Springer-Verlag, 1980).

[41] M. Bender, P.-H. Heenen, and P.-G. Reinhard, Self-consistent mean-field models for nuclear structure, Rev. Mod. Phys. **75**, 121 (2003).

[42] J. Menéndez, N. Hinohara, J. Engel, G. Martínez-Pinedo, and T. R. Rodríguez, Testing the importance of collective correlations in neutrinoless $\beta\beta$ decay, Phys. Rev. C **93**, 014305 (2016).

[43] T. R. Rodríguez and G. Martínez-Pinedo, Energy density functional study of nuclear matrix elements for neutrinoless $\beta\beta$ decay, Phys. Rev. Lett. **105**, 252503 (2010).

[44] T. R. Rodríguez and G. Martínez-Pinedo, Neutrinoless $\beta\beta$ decay nuclear matrix elements in an isotopic chain, Phys. Lett. B **719**, 174 (2013).

[45] J. M. Yao, B. Bally, J. Engel, R. Wirth, T. R. Rodríguez, and H. Hergert, Ab initio treatment of collective correlations and the neutrinoless double beta decay of $^{48}$Ca, Phys. Rev. Lett. **124**, 232501 (2020).

[46] J. M. Yao, J. Engel, L. J. Wang, C. F. Jiao, and H. Hergert, Generator-coordinate reference states for spectra and $0\nu\beta\beta$ decay in the in-medium similarity renormalization group, Phys. Rev. C **98**, 054311 (2018).

[47] L. S. Song, J. M. Yao, P. Ring, and J. Meng, Nuclear matrix element of neutrinoless double-$\beta$ decay: Relativity and short-range correlations, Phys. Rev. C **95**, 024305 (2017).

[48] J. M. Yao, L. S. Song, K. Hagino, P. Ring, and J. Meng, Systematic study of nuclear matrix elements in neutrinoless double-$\beta$ decay with a beyond-mean-field covariant density functional theory, Phys. Rev. C **91**, 024316 (2015).

[49] L. S. Song, J. M. Yao, P. Ring, and J. Meng, Relativistic description of nuclear matrix elements in neutrinoless double-$\beta$ decay, Phys. Rev. C **90**, 054309 (2014).

[50] C. F. Jiao, J. Engel, and J. D. Holt, Neutrinoless double-$\beta$ decay matrix elements in large shell-model spaces with the generator-coordinate method, Phys. Rev. C **96**, 054310 (2017).

[51] C. F. Jiao, M. Horoi, and A. Neacsu, Neutrinoless double-$\beta$ decay of $^{124}$Sn, $^{130}$Te, and $^{136}$Xe in the hamiltonian-based generator-coordinate method, Phys. Rev. C **98**, 064324 (2018).

[52] C. Jiao and C. W. Johnson, Union of rotational and vibrational modes in generator-coordinate-type calculations, with application to neutrinoless double-$\beta$ decay, Phys. Rev. C **100**, 031303(R) (2019).